Copper-manganese oxide catalysts for low-temperature oxidation of indoor pollutants

Applied Catalysis B: Environment and Energy 385 (2026) 126292

Contents lists available at ScienceDirect

Applied Catalysis B: Environment and Energy

journal homepage: www.elsevier.com/locate/apcatb

Copper-manganese oxide catalysts for low-temperature oxidation of indoor pollutants

Nadia Grifasi [a], Enrico Sartoretti [a], Piotr Legutko [b], Samir Bensaid [a], Nunzio Russo [a], Andrzej Adamski [b], Debora Fino [a], Marco Piumetti [a,*]

[a] Department of Applied Science and Technology, Polytechnic of Turin, Corso Duca Degli Abruzzi, 24, Turin 10129, Italy
[b] Faculty of Chemistry, Jagiellonian University, Gronostajowa 2, Kraków 30-387, Poland

ARTICLE INFO

Keywords:
VOCs abatement
Indoor air purification
CO oxidation
Copper - Manganese oxide
Nanostructured oxide catalysts

ABSTRACT

Indoor air purification is crucial for preserving health and well-being in enclosed spaces. This study presents the successful low-temperature oxidation of CO and ethylene, considered as indoor air pollutants, achieved without employing expensive precious metals. A series of binary $CuMnO_x$ samples, with a Cu/(Cu+Mn) ratio of 15 wt%, were prepared using various synthesis procedures and thoroughly characterized to understand their physico-chemical and their link with catalytic properties. The findings revealed that copper significantly enhanced the performance of all samples when compared to the pure MnO_x materials. For all the pollutants investigated, the best-performing catalyst was the Cu-Mn mixed oxide obtained through a redox route, which achieved complete CO oxidation at room temperature and maintained high activity for over 250 h. For ethylene, it demonstrated superior low-temperature catalytic oxidation compared to the other samples, reaching a T_{10} equal to 85 °C. These remarkable performances were attributed to enhanced oxygen mobility, increased reducibility, and the synergy between copper and manganese, which played a pivotal role in VOC oxidation. Notably, long-term stability tests under continuous flow, variation of GHSV, pollutant and oxygen concentrations, and catalytic performance under wet conditions confirmed the excellent durability and versatility of the catalyst, even at extremely low catalyst loadings. Further catalytic testing and spent catalyst analysis revealed that the low-temperature oxidation mechanism involves a Mars-van Krevelen-like reaction pathway with parallel involvement of both reactive surface oxygen species and molecular oxygen, all of which play a crucial role in the reaction process. Finally, this work provides a systematic correlation between catalytic activity (in terms of both T_{100} and reaction rate) and structural, redox, acid-base, and electronic properties, demonstrating that the decisive factors differ for CO and C_2H_4 oxidation.

1. Introduction

In recent years, the issue of indoor air pollution has gained significant attention [1]. The most common gaseous pollutants in indoor environments are Volatile Organic Compounds (VOCs) and inorganic molecules (e.g., CO). These substances are considered highly dangerous for the environment and human health due to their volatility, ease of diffusion, and potential toxicity [2–4]. Such pollutants come from various sources within indoor spaces, including building materials, furniture, cleaning products, air fresheners, tobacco smoke, and even cooking activities [4]. Prolonged exposure to VOCs can lead to many negative symptoms like eye and throat irritation, headaches, dizziness, nausea, and, in more negative scenarios, they can contribute even to serious dysfunctions of such organs as the liver, kidneys, and nervous system [3,4]. Of course, the negative effects of poor indoor air quality depend on various factors, such as the type and concentration of pollutants, their interactions with other chemicals, the duration of exposure, and the vulnerability of the people exposed. As a result, stricter regulations have been enacted to manage VOC emissions indoors, although these laws differ significantly from one country to another. In the U.S., the ANSI/ASHRAE 62.1 standard provides guidelines for ventilation rates in various indoor settings, but it does not specify limits on pollutant concentrations. In contrast, several European countries have developed specific legislation and standards for pollutants. Similar regulations also exist in other parts of the world, such as China, where the “Code for Indoor Environmental Pollution Control of Civil Building

* Corresponding author.
E-mail address: marco.piumetti@polito.it (M. Piumetti).

https://doi.org/10.1016/j.apcatb.2025.126292
Received 10 August 2025; Received in revised form 27 November 2025; Accepted 6 December 2025
Available online 7 December 2025

Engineering" has been implemented [5–8].

To ensure better health and safety in indoor environments, the removal of indoor pollutants has become a priority, leading to the development of various purification technologies. Some of these technologies include purging, biological filtration, photocatalytic oxidation (PCO), thermal catalytic oxidation, and plasma treatment [2,9–11]. Besides the other air purification methods based often on sorption, catalytic methods, including oxidation at low or moderate temperatures, stand out as effective and promising solutions for the complete removal of indoor VOCs. This is due to the relatively high economic viability of these methods and the ability to work at lower temperatures with controlled and satisfactory selectivity. In this context, noble metal catalysts have been widely applied in catalytic oxidation reactions because of their outstanding catalytic activity and stability. For instance, Gu et al. [12] synthesized an Au/MnO_2 sample and tested it for CO oxidation. This catalyst was extremely active at a very low temperature (even below 0 °C), and highly stable at 25 °C for many hours under normal conditions. Wang et al. [13] functionalized different manganese supports and observed substantial changes in CO oxidation activity with the following trend: $Au/Mn_2O_3 > Au/MnO_2 > Au/Mn_3O_4$, leading to a complete CO removal at room temperature. Yang et al. [14] synthesized Pt/ZSM-5 and evaluated its performance for the oxidation of 100 ppm of ethylene in the presence of 21 vol% O_2, reaching complete oxidation of this pollutant at room temperature. In another work, Chen et al. [15] encapsulated Pd NPs in TS-1 zeolite for catalytic abatement of indoor formaldehyde at room temperature. However, the high cost and limited availability of the precious metal catalysts represent an important limitation for their commercialization [16]. Hence, a main challenge lies in developing noble metal-free materials that perform exceptionally well at low temperatures (such as room temperature) so they can be effectively used in indoor environments.

In this context, manganese oxides have been largely investigated due to their attractive physico-chemical properties, different valence states of Mn, and tendency to give rise to structural defects [17–19]. These features make them particularly suitable for low/middle-temperature applications. Depending on the preparation method (hydrothermal, redox methods, sol-gel, etc.), a variety of structures or morphologies can be obtained (i.e., β-MnO_2, γ-MnO_2, α-Mn_2O_3, α-Mn_3O_4), showing diverse catalytic activity due to the preferential exposure of different active sites [20,21]. In our previous work [17], we observed that catalysts synthesized through solution combustion synthesis exhibited the best catalytic performance toward CO, ethylene, and propylene, compared to the nanocasting procedure. Moreover, the synergy between different crystalline phases (mainly β-MnO_2, R-MnO_2, and Mn_2O_3) increased the quantity and variety of structural defects, creating a very reactive material with a higher surface concentration of Mn^{4+} and active oxygen species. However, the temperature to completely oxidize the pollutants (mainly CO, ethylene, and propylene) was still quite high (higher than 100 °C and 200 °C for CO and ethylene, respectively). In the literature [22–24], it is reported that the inclusion of a small amount of another element (e.g., Cu) in the structure of manganese oxides could enhance the catalytic performance of MnO_x-based catalysts at low temperatures. Although copper oxides alone have poor catalytic performance compared to MnO_x [22,24,25], the synergy between Cu and Mn in the binary catalyst structure could boost and significantly affect catalytic activity. Certainly, the preparation methods, Cu-to-Mn ratio, drying temperature, and calcination conditions can strongly affect the catalytic performance of $CuMnO_x$ materials [23,25,26]. Specifically, extreme importance should be given to the copper-manganese ratio, which is confirmed as a key parameter controlling reactivity. Various authors [16,22,23,27] reported an optimum copper concentration ranging from 9 to less than 20 wt%, with an optimum between 10 and 15 wt%. In fact, higher concentrations lead to phase segregation and a loss of reactive oxygen species, whereas too-low concentrations are associated with no tangible effects. Although this range is not universally valid, it has been consistently reported for CuMn-based systems, prepared through different synthesis routes, that a Cu/(Cu+Mn) loading of around 15 wt% may represent a balanced compromise content for catalytic applications involving the oxidation of both CO and VOCs, such as ethylene. Detailed state-of-the-art research was summarized in Table S1. For instance, previous studies on redox-based $CuMnO_x$ catalysts reported the best activity for CO oxidation at approximately 9 wt% total Cu [23], while other works highlighted that lower Cu loadings (5–10 wt%) are often sufficient for catalysts tested in CO oxidation but less effective for those tested in ethylene oxidation, and higher Cu loadings (>20 wt%) tend to cause CuO segregation and a decrease in catalytic performance [27].

Based on these premises, three different synthesis procedures (i.e., solution combustion synthesis, oxalate route, and redox route) were employed here to obtain extremely active $CuMnO_x$ samples with a nominal copper loading of 15 wt% (in terms of Cu/(Cu+Mn)), without introducing compositional variability. These materials were designed to exhibit enhanced stability over time in the presence of the tested pollutants. In this work, the attention was focused on the oxidation of CO and ethylene. The content of 15 wt% Cu/(Cu+Mn) was selected for this study to ensure a balanced catalytic response toward both pollutants. Specifically, carbon monoxide is one of the most common gaseous pollutants detected in confined spaces. It is a highly dangerous and toxic gas, generally emitted from incomplete combustion processes. The main indoor sources of CO are tobacco smoke, defective cooking, and heating devices, in addition to outdoor air exchange in dense traffic areas or highly industrialized districts [11]. On the other hand, ethylene is a natural ripening hormone of plants. Other sources include automotive emissions, plastics, smoke, and fluorescent lights [28]. Even small amounts of ethylene (from ppb to ppm) during storage can cause a faster deterioration of fresh products. In addition, ethylene exposure may have some deleterious effects on human health, provoking asthma and allergies [29]. However, there is a lack of information concerning efficient ways of removing it from confined spaces and extremely diluted gas mixtures.

The main aim of this study is to offer new perspectives on how the presence of copper influences the performance of manganese oxides, resulting in the creation of highly defective and reactive structures. The research focuses on the critical role of redox properties and the influence of reactive oxygen species and molecular oxygen, linking them to the catalytic performance in the complete oxidation of various gaseous pollutants. Furthermore, a comprehensive correlation is proposed between catalytic performance (in terms of T_{100} and reaction rates) and structural, redox, acid-base, and electronic properties, revealing that the parameters governing the oxidation of CO and ethylene are different, an aspect rarely explored in the literature. In addition, the work function was proposed as a useful electronic descriptor for $CuMnO_x$ systems, establishing for the first time a relationship between this parameter and catalytic activity. The results obtained lay the foundation for developing commercially viable catalysts prepared via simple, cost-effective, and rapid synthesis procedures that can also be used in indoor environments.

2. Materials and methods

2.1. Catalyst preparation

All the reagents used in the synthesis procedures were employed without any further purification. Milli-Q water; manganese nitrate tetrahydrate ($Mn(NO_3)_2$ 4 H_2O, > 97 %, Merck); urea (ACS reagent, 99–100.5 %, Sigma-Aldrich); copper nitrate tetrahydrate ($Cu(NO_3)_2$ 4 H_2O, > 99 %, Merck); oxalic acid ($H_2C_2O_4$, >99 %, Merck); ammonia solution (NH_3 H_2O, 28–30 %, Merck); potassium permanganate ($KMnO_4$, >99 %, Merck); manganese acetate ($Mn(CH_3COO)_2$, > 99 %, Merck);

Different procedures (described below) were adopted for the synthesis of the $CuMnO_x$ samples. In all cases, the Cu/(Cu+Mn) ratio was kept constant and equal to 15 wt%.

2.1.1. Oxalate route

The oxalate route was employed to obtain materials of a high specific surface area. The procedure proposed by Frey et al. [30] and Iablokov et al. [31] was carefully modified to achieve the desired characteristics. Specifically, the desired amounts of $Mn(NO_3)_2$ and $Cu(NO_3)_2$ were added to a solution of oxalic acid (0.06 M) to obtain a Cu/(Cu+Mn) ratio of 15 wt% in the final oxide. The mixing step proved to be crucial and caused a color change. Then, a proper amount of ammonia solution was added dropwise until the pH reached the value 8. The solution was kept under stirring for 50 min at room temperature, after which it was centrifuged, washed with water, and dried at 70 °C. Finally, the sample was calcined in an oven under an air atmosphere at 360 °C, with a heating rate of 5 °C min^{-1} for 10 min. The resulting sample was denoted $CuMnO_x$_oxalate. For comparison, the respective manganese oxide was synthesized without adding the copper precursor, following the same procedure as the one described above. This sample was denoted MnO_x_oxalate.

2.1.2. Solution combustion synthesis (SCS)

The SCS technique is a very simple and rapid synthesis method for obtaining highly defective and active materials at low temperatures. Specifically, the MnO_x_SCS sample was synthesized following the procedure described in our previous work [17], which led to obtaining the catalyst with the best catalytic performance. To prepare the copper-doped sample, the procedure was modified by adding the desired amount of $Cu(NO_3)_2$ to the aqueous solution of $Mn(NO_3)_2$. After 10 min of stirring at room temperature, the urea, used as fuel (molar ratio 0.4), was added, and the final solution was transferred to an oven for calcination at 400 °C for 10 min, with a heating rate of 5 °C min^{-1}. Finally, the powder was rinsed with water to remove impurities and dried at 60 °C. The resulting sample was denoted $CuMnO_x$_SCS.

2.1.3. Redox route

The redox route was employed to obtain amorphous materials with a high specific surface area and high defectiveness. The procedure proposed by Njagi et al. [23] was adapted to prepare controlled structural/morphological features. In a typical synthesis, two aqueous solutions of $KMnO_4$ (Sol. A) and $Mn(CH_3COO)_2$ with $Cu(NO_3)_2$ (Sol. B) were synthesized separately, using an ultrasound bath to guarantee good solid dissolution at this stage. After that, Sol. B was slowly added to Sol. A, under vigorous stirring at room temperature. The final solution was kept under stirring for 24 h. Subsequently, it was centrifuged and rinsed several times to achieve a pH close to neutrality. After drying at 70 °C for 48 h, the powder was calcined at 300 °C for 2 h, with a heating rate of 5 °C min^{-1}. The sample was denoted $CuMnO_x$_redox. For comparison, the respective MnO_x sample without copper was synthesized by following the same procedure. This catalyst was named MnO_x_redox. More details concerning the characterization of the dried sample and the calcined one were reported in Figure S1 in the Supporting Information.

2.2. Catalysts characterization

To assess the textural properties, such as specific surface area (SSA, m^2 g^{-1}), total pore volume (VTP, cm^3 g^{-1}), and pore diameter (D_p), N_2 physisorption at −196 °C was conducted with a Micromeritics Tristar II 3020 (v1.03, Micromeritics Instrument Corp.). Before starting the measurement, the powders were degassed under nitrogen flow at 200 °C for 2 h to remove surface contaminants. The SSA was determined using the Brunauer-Emmett-Teller (BET) method, while the VTP and Dp were obtained via the Barrett-Joyner-Halenda (BJH) method during the desorption step.

The crystalline structure of the samples was analyzed using powder X-ray diffraction (XRD). The diffraction patterns were recorded using an Empyrean Panalytical X'Pert PRO diffractometer, with Cu K_α radiation (2θ range = 10°–90°; step size = 0.013° 2θ; acquisition time per step = 118.3 s). The collected diffraction peaks were compared to the Powder Data File (PDF-2004, International Centre for Diffraction Data), and the average crystallite size was determined using Scherrer's equation [32]. Moreover, to investigate the stability of the samples, variable-temperature XRD measurements were performed on the same apparatus using an HTK 1200 N heating chamber (Anton Paar). The diffractograms were collected from room temperature up to 200 °C under an air atmosphere in the 2θ range of 10° – 90°.

To better investigate the structure of the catalysts, micro-Raman spectra were obtained under ambient conditions using a Renishaw InVia Qontor Raman Confocal Microscope equipped with a Leica DMLM confocal microscope and a CCD detector, employing an excitation wavelength of 532 nm and 785 nm. The laser power at the sample position was set at 0.1–10 % of the total power with a magnification of 50 times (optimized for the undoped samples). The Raman scattered light was collected across the spectral range of 100–1300 cm^{-1}. To guarantee an ample signal-to-noise ratio, 512–1024 scans were accumulated. The Raman spectra were deconvoluted using PeakFit (v4.12) software.

The internal structure of the samples was studied by high-resolution transmission electron microscopy (HR-TEM, Talos F200X, Thermo Scientific) with a LaB_6 electron gun, operating at 200 kV. A small amount of powder was dispersed in isopropanol, sonicated for 15 min at room temperature, and then applied to nickel grids coated with lacey carbon films. The images obtained were processed using ImageJ software. An energy-dispersive X-ray (EDX) analysis was performed on the same apparatus to verify the copper content. Spectra were collected from at least five different locations on each sample to assess the homogeneity of the material.

To investigate the elemental composition and oxidation states of the elements present at the surface of the materials, X-ray photoelectron spectroscopy (XPS) was performed on an Omicron Argus X-ray photoelectron spectrometer, equipped with a monochromated AlKα radiation source (hν = 1486.6 eV). The spectra were deconvoluted using Casa XPS v.2.3.16 software (Casa Software Ltd, U.K.) and applying a Gaussian/Lorentzian ratio g/l equal to 70/30 for deconvolution.

The reducibility of the studied catalysts was evaluated through temperature-programmed reduction (H_2-TPR) using an ALTAMIRA AMI300 Lite TPD/R/O system with a thermal conductivity detector (TCD). Initially, 30 mg of the sample powder was placed in a quartz U-tube reactor and pretreated with a flow of 20 mL min^{-1} of pure He at 250 °C for 1 h. After cooling to 50 °C, a reducing gas mixture of 5 H_2/Ar was introduced at a flow rate of 20 mL min^{-1}. The temperature was increased from 50 °C to 700 °C at a rate of 5 °C min^{-1}, and the final temperature was maintained for 30 min. H_2-uptake was evaluated using CuO as a standard. The detailed procedure to evaluate the H_2-uptake is reported in the Supporting Information. To investigate oxygen mobility, O_2-TPD analyses were performed on the same instrument. Precisely, 30 mg of sample was pretreated under a pure O_2 flow (40 mL min^{-1}) for 2 h at 250 °C. After cooling down to 50 °C, the analysis started by flowing 20 mL min^{-1} of pure He and heating to 600 °C with a heating ramp of 5 °C min^{-1}. Finally, the acidity of the copper-containing samples was investigated through temperature-programmed desorption of ammonia (NH_3-TPD) carried out on the same instrument. After a preliminary pretreatment under He flow at 250 °C for 2 h, 20 mL min^{-1} of a mixture containing 10 % NH_3/He was fed to 30 mg of sample at 100 °C for 1 h. After that, the analysis was carried out by heating the sample to 600 °C with a heating ramp of 5 °C min^{-1} under a 20 mL min^{-1} flow of He. The detailed procedure to evaluate the quantity of O_2 and NH_3 desorbed is reported in the Supporting Information.

Finally, for the evaluation of electronic properties, the Kelvin Probe (McAllister KP6500) was used. The contact potential difference (V_{CPD}) measurements were carried out by the dynamic condenser method of Kelvin. For each sample, the first measurement was performed in ambient conditions, and the second was carried out in a vacuum (10^{-7} mbar) at 150 °C after annealing the sample to 500 °C. The work function values were obtained from a simple relation ($eV_{CPD} = \Phi_{reference} - \Phi_{sample}$), using a standard stainless-steel plate as a reference electrode (d = 3 mm,

$\Phi_{reference} = 4.1$ eV).

2.3. Catalytic tests

Catalytic oxidation experiments were carried out in a fixed-bed quartz U-shaped reactor (ID = 4 mm) heated by a PID-controlled furnace. The temperature within the bed was continuously monitored using a K-type thermocouple placed inside the reactor. In a typical procedure, 50 mg of catalyst powder was pretreated by flowing pure N_2 (100 mL min^{-1}, 150 °C, 1 h) to desorb moisture and physisorbed compounds. Once the system cooled to room temperature, a reactive gas mixture simulating indoor air conditions was introduced into the reactor at a flow rate of 50 mL min^{-1}. This mixture contained 100 ppm of pollutant (either CO or ethylene as target noxious agents), 21vol.% O_2, and the balance of N_2. The concentration of pollutants was chosen considering the maximum allowed value in confined spaces [33]. All the experiments were conducted using a constant catalyst weight-to-volumetric flow rate ratio (W F^{-1}) of 0.017 g h L^{-1}. The test began at room temperature and the outlet gas composition was continuously monitored using a non-dispersive infrared (NDIR) gas analyzer (ABB Uras 14, ABB S.p.A., PAMA, Milan, Italy) connected to the outlet of the reactor. The temperature gradually increased with an isothermal step every 25 °C to avoid the influence of adsorption-desorption phenomena. The test was considered complete when the pollutant conversion reached 100 %. The catalytic activity of the samples was compared in terms of conversion rates evaluated in the kinetic regime (conversion < 30 %) and in terms of T_{10}, T_{50}, T_{90}, and T_{100}, which correspond to the temperatures at which 10 %, 50 %, 90 %, and 100 % conversion were achieved, respectively.

The most efficient catalyst was also tested by performing time-on-stream (TOS) analyses to assess the catalytic stability of the catalysts for several hours under reaction conditions. Moreover, the influence of gas hourly space velocity GHSV, which is defined as the volumetric flow rate of the feed gas divided by the catalyst bed volume, was also investigated by varying it in the range between $5{\cdot}10^3$ - $240{\cdot}10^3$ h^{-1}, by feeding the same gas composition already described. Further tests with different pollutant concentrations (100–1000 ppm), the influence of oxygen in the gas mixture (0–21 vol%), and the simultaneous presence of different pollutants (100 ppm CO and 100 ppm ethylene in the same gas mixture) were also investigated to study the effects on the performance of the best-performing catalyst. Finally, tests under wet conditions were also carried out for both CO and ethylene, feeding a polluted mixture fully saturated with water at room temperature.

2.4. Reaction mechanism

To investigate the reaction mechanism more in-depth, *in-situ* DRIFTS experiments were conducted using a Praying Mantis™ Diffuse Reflectance Accessory, equipped with Praying Mantis™ High-Temperature Reaction Chambers. The outlet was connected with a Hiden QGA quadrupole mass spectrometer. The detailed procedure is reported in Scheme 1 in the Supporting Information.

Spectra recorded over time and temperature were acquired using a Bruker Invenio S spectrometer, featuring a liquid N_2-cooled MCT detector, with a resolution of 2 cm^{-1}, using 64 scans over the spectral range of 400–4000 cm^{-1}. KBr powder, previously dried under N_2 flow at 200 °C and atmospheric pressure, was used as a reference for the background spectrum. Opus software (v. 8.2) was employed to elaborate the recorded spectra.

3. Results and discussion

3.1. Physico-chemical characterization results

The textural parameters obtained for all the investigated samples from N_2-physisorption performed at −196 °C were summarized in Table 1 and presented in Figure S2. All investigated the samples exhibited type-IV isotherms, which are characteristic of mesoporous materials. This finding remains in line with previous literature reports [17,31]. Following the nomenclature defined by IUPAC [34], most of the samples exhibited an H3-type hysteresis loop, which is typically observed in the case of materials with irregular or intersecting pore shapes. This could suggest that the materials may have non-uniform, complex pore structures. Additionally, for both the oxalate route and SCS-synthesized samples, the incorporation of copper into the MnO_x structures did not cause any significant changes in the shape of the isotherms. However, the SSA and pore diameter values were affected by that, as shown in Table 1. In contrast, the samples synthesized via the redox route exhibited more pronounced textural differences. Specifically, MnO_x_redox displayed a hysteresis loop corresponding to H1, which is associated with materials having uniform or monodisperse pores, as evidenced by the pore size distribution shown in Figure S2. Upon adding copper into the structure, the shape of the corresponding isotherm was altered, and the hysteresis loop became similar to that of the other investigated samples, indicating a shift towards a more complex pore structure. This was also valid for the sample that did not undergo to calcination step (see Figure S1). Furthermore, as previously mentioned, the presence of copper in the samples significantly increased the SSA compared to the respective copper-free samples synthesized via the same method. Specifically, the oxalate route technique provided the highest SSA value (356 m^2 g^{-1}), followed by those determined for samples obtained by the redox (329 m^2 g^{-1}) and SCS (45 m^2 g^{-1}) methods. Generally, with the increase in surface area, a corresponding increase in pore volume was also observed, along with a reduction in pore size.

Table 1
Textural properties and crystallite sizes of the samples, evaluated from the N_2 physisorption at −196 °C and XRD patterns.

Sample	SSA[a] (m^2g^{-1})	VTP[b] (cm^3 g^{-1})	Dp[b] (nm)	Crystallite size[c] (nm)
MnO_x_SCS	36	0.100	13.3	7.9
$CuMnO_x$_SCS	45	0.159	10.9	5.3
MnO_x_oxalate	183	0.249	8.2	7.2
$CuMnO_x$_oxalate	356	0.312	6.3	3.5
MnO_x_redox	247	0.470	6.6	4.7
$CuMnO_x$_redox	329	0.602	7.6	2.4

[a] Specific surface area (SSA) evaluated according to the Brunauer-Emmett-Teller (BET) method
[b] Total pore volume (VTP) and average pore diameter (Dp) evaluated according to the Barrett-Joyner-Halenda (BJH) method during the desorption phase
[c] Crystallite sizes evaluated according to Scherrer's formula [32]

The diffraction patterns of all the samples are illustrated in Fig. 1**A**, while their crystallite size is reported in Table 1. By comparing all the samples investigated in this work, it appeared that the presence of copper reduced the initial crystallinity of MnO_x structures. In fact, in the case of doped samples, the XRD maxima were broader and exhibited much lower intensity compared to their respective pure MnO_x counterparts. Furthermore, when comparing the various synthesis techniques, only the oxalate route allowed for the formation of well-defined XRD patterns. In all other cases, the samples appeared to be poorly crystalline, indicating a strong contribution of amorphous components in the final phase composition, as also observed in the TEM images (see later). When comparing the samples synthesized using the same method, namely the corresponding undoped and copper-containing catalysts, it was evident that the presence of copper in the structure not only modified the intensity and the area of the peaks but also caused a small shift toward lower angles. This can be explained from the perspective of the atomic radius. Indeed, the ionic radius of copper is 73 pm, while that of manganese is around 46 pm [35]. However, this shift was not very prominent due to the low amount of copper in the structure.

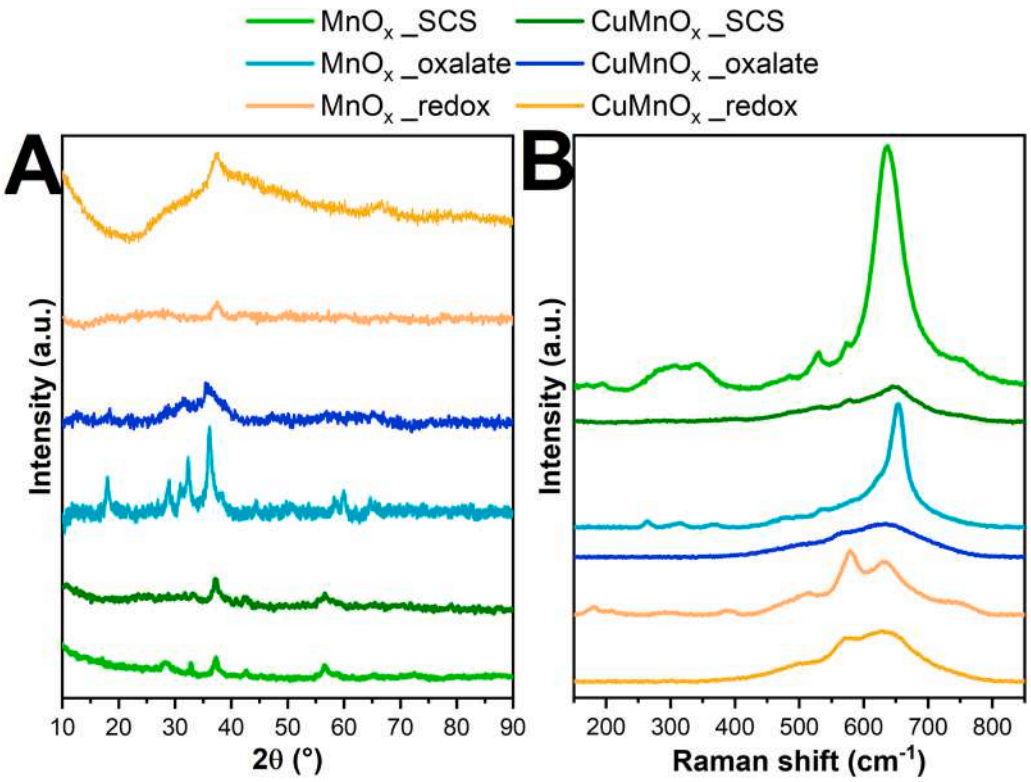

Fig. 1. X-ray diffraction patterns (A) and Raman spectra (B) of MnO_x and $CuMnO_x$ samples.

From the elaboration of the XRD diffractograms, it was possible to deduce both the phase composition of the samples studied and their crystallinity (Figure S3). Regarding the materials obtained via the oxalate route, the undoped MnO_x_oxalate sample exhibited distinctly higher crystallinity compared to the Cu-doped sample. Specifically, it displayed Mn_3O_4 as the main crystalline phase, following the reference patterns in the PDF database (01–075–1560), with the most intense Bragg maxima located at $2\theta = 36.13°$ (2 1 1) and 32.32° (1 0 3). On the other hand, the doped $CuMnO_x$_oxalate sample revealed the presence of $CuMnO_2$ as the main crystalline phase (reference pattern 01–075–1010), with its most intense maxima at 35.46° (-1 1 1) and 31.40° (2 0 0). The presence of other maxima of significantly lower intensity was also detected, which can be attributed to the presence of $CuMn_2O_4$ phase (reference pattern 01–074–2422) giving rise to the maximum located at 18.50° (1 1 1) and Mn_3O_4 (reference pattern 01–075–1560), contributing to the Bragg maxima for the peaks at 28.80° (1 1 2) and 58.31° (3 2 1).

Concerning the SCS method, the MnO_x_SCS sample exhibited MnO_2 as the main crystalline phase, with maxima ascribed to both the pyrolusite phase with a tetragonal structure (reference pattern 01–071–0071) and the ramsdellite phase of an orthorhombic structure (reference pattern 01–082–2169), in line with our previous work [17]. Moreover, this sample displayed the presence of a single Bragg maximum ascribed to the Mn_2O_3 crystalline phase of an orthorhombic structure (reference pattern 01–071–0635), as a small impurity. For the $CuMnO_x$_SCS sample, the peaks were slightly shifted toward lower angles for the same reason as previously described. In this case, the main crystalline phase was $CuMnO_2$ (reference pattern 01–075–1010), with the most intense patterns at 36.96° (-1 1 1) and 56.66° (-1 1 3). A small admixture of MnO_2 was also detected and attributed to the maximum at 42.61° (1 1 1).

Finally, the samples synthesized via the redox route showed the lowest crystallinity and a higher content of amorphous phase. The XRD patterns recorded were in line with the literature [23]. Specifically, the MnO_x_redox sample exhibited the same crystalline phases of the same nature as detected for the MnO_x_SCS sample, however, with much less intense Bragg maxima. In contrast, the $CuMnO_x$_redox sample was the only one that displayed quite intense maxima associated with the presence of $CuMn_2O_4$ (reference pattern 01–074–2422). The other weak maxima observed in the corresponding XRD pattern belonged to the $CuMnO_2$ phase component (reference pattern 01–075–1010).

In conclusion, no maxima related to the presence of segregated CuO oxide were detected, demonstrating that copper was well incorporated into the MnO_x structures, and no phase separation occurred. This assumption was also confirmed by the recorded EDX maps. Finally, the size of the crystallites was evaluated using the Scherrer equation [32], and the results were reported in Table 1. As a whole, the presence of copper in the structure not only favored an amorphization of the doped samples, causing a partial loss of crystallinity, but was also responsible for the associated broadening of the diffraction lines and the reduction of the crystallite sizes. In fact, the MnO_x samples, in all cases, showed larger crystallites, with diameters of 7.9, 7.2, and 4.7 nm for MnO_x_SCS, MnO_x_oxalate, and MnO_x_redox, respectively. In contrast, the doped samples exhibited distinctly smaller crystallites (5.3, 3.5, and 2.4 nm for $CuMnO_x$_SCS, $CuMnO_x$_oxalate, and $CuMnO_x$_redox, respectively). This could affect catalytic performance, since smaller crystallites often lead to a higher surface area and can expose a greater number of catalytically active sites, thus making the oxide more reactive [36,37].

Raman analysis was carried out to investigate the structure of not only the crystalline but also the amorphous phases in more detail. Overall, the recorded spectra provided valuable insight into how synthesis routes and doping with copper influenced the structural order of manganese oxides. The results were reported in Fig. 1**B** and Figure S4 and were consistent with the findings of XRD and TEM (see below). The strong Raman bands between 630 and 660 cm^{-1} were ascribed to the stretching vibrations of Mn-O on the [MnO_6] octahedron [38]. The peaks between 250 and 350 cm^{-1} corresponded to the mode associated with translational motion of the MnO_6 octahedrons and bending vibration of the Mn-O bonds, respectively [39,40]. The detailed assignment of Raman peaks was reported in Table 2.

The most interesting structural feature manifested in the recorded

Table 2
Positions and attributions of the peaks present in deconvoluted Raman spectra of the MnO_x and $CuMnO_x$ samples.

Sample	Maximum position (cm^{-1})	Attribution	Reference
MnO_x_SCS	308	ν_2 of R-Mn_2O_3	[38]
	344	ν_2 of λ-MnO_2 (β+R)	
	530	ν_5 of β-MnO_2	
	573	ν_5 of λ-MnO_2 (β+R)	
	636	ν_6 of R-MnO_2	
	750	ν_8 of β-MnO_2	
$CuMnO_x$_SCS	529	ν5 of β-MnO_2	[38]
	572	$CuMnO_2$	[41]
	575	ν_5 of λ-MnO_2 (β+R)	[38]
	649	$CuMnO_2$	[41]
	748	ν_8 of β-MnO_2	[38]
MnO_x_redox	389	Torsional vibrations of Mn-O	[42,43]
	513	(α-MnO_2, cryptomelane)	[42,43]
	579	vibrations of the Mn-O units in the 2 × 2 tunnels of the A_g symmetry (α-MnO_2, cryptomelane)	[42,43]
	616	A_{1g}, stretching mode of MnO_6 octahedra in λ-MnO_2	[38]
	634	ν_6 of R-MnO_2vibrations of the Mn-O units in the 2 × 2 tunnels of the A_g symmetry (α-MnO_2, cryptomelane)	[38,42, 43]
	746	bending vibrations of Mn-O (α-MnO_2, cryptomelane) or ν_8 of β-MnO_2	[38,42, 43]
$CuMnO_x$_redox	499	(α-MnO_2, cryptomelane)	[42,43]
	571	$CuMnO_2$	[41]
	621	$CuMn_2O_4$	[44]
	636	ν_6 of R-MnO_2vibrations of the Mn-O units in the 2 × 2 tunnels of the A_g symmetry (α-MnO_2, cryptomelane)	[38,42, 43]
	746	bending vibrations of Mn-O (α-MnO_2, cryptomelane)	[42,43]
MnO_x_oxalate	264	ν_1 of γ-Mn_2O_3	[38]
	312	ν_2 of Mn_3O_4	
	368	ν_2 of Mn_3O_4	
	482	ν_4 of Mn_3O_4	
	534	ν_5 of γ-Mn_2O_3	
	583	ν_5 of Mn_3O_4	
	654	ν_9 of Mn_3O_4	
$CuMnO_x$_oxalate	528	ν_7 of Mn_3O_4	[38]
	565	$CuMnO_2$	[41]
	621	$CuMn_2O_4$	[44]
	649	$CuMnO_2$	[41]

Raman spectra, compared to that observed for undoped and copper-containing samples, was that substantial modifications of the local environment of manganese sites occur in the binary structures due to the presence of copper centers. Incorporation of copper into MnO_x lattices substantially altered distances within the cationic sublattice and modified the strength of the local electrostatic field. These effects provoked visible changes in terms of intensity and shifts of the corresponding bands in the recorded Raman spectra (Figure S4). Specifically, the samples synthesized via the SCS method displayed sharper and more intense Raman peaks, indicating a better crystallinity and more ordered local structure, which remained in agreement with the reported XRD results, analysis of crystallite sizes, and TEM images. Simultaneously, the recorded Raman spectra reflected not only structural differences in MnO_x induced by the presence of copper dopant but also those induced by different synthetic routes. In contrast, the samples prepared by the oxalate and redox methods showed broader and less intense peaks, suggesting a more disordered and amorphous structure. Specifically, a shift to lower wavenumbers could indicate a weakening of the Mn-O interactions ($CuMnO_x$_SCS (645 cm^{-1}) > $CuMnO_x$_oxalate (634 cm^{-1}) > $CuMnO_x$_redox (630 cm^{-1})). The shift of these peaks from 645 to 630 cm^{-1} may reflect the interaction of CuO with Mn_2O_3, leading to the formation of Cu-O-Mn structures at the interface between CuO and Mn_2O_3, and simultaneously favoring strong local interactions between Cu^{2+} and Mn^{3+} [45].

To assess the structural stability of the copper-containing catalysts under reaction conditions, variable-temperature XRD measurements were carried out in air within the operational temperature range from 25 to 200 °C. The collected patterns, shown in Fig. 2, revealed no significant changes in the diffraction profiles with increasing temperature. Specifically, no shifts in peak positions, variations in peak intensity, or the appearance of new diffraction maxima were observed. This indicated that the crystalline structure of all the samples remained unchanged and structurally stable under the operating conditions investigated. Variable-temperature XRD measurements were also performed on the dried $CuMnO_x$_redox sample for comparison purposes. As evidenced in Figure S1, no changes occurred in the structure. However, DRIFTS measurements and temperature-programmed oxidation experiments suggested the presence of some residues of synthesis that were not present in the calcined sample (see Figure S1).

TEM analysis was performed to deeply investigate the internal structure of the samples. As can be seen in Fig. 3, the $CuMnO_x$_redox sample exhibited an extremely amorphous structure, as also revealed by the XRD analysis. However, it was possible to identify some small crystalline domains ascribed to the presence of both $CuMnO_2$ and $CuMn_2O_4$ crystalline phases. Specifically, interplanar distances of 0.275 nm and 0.240 nm ascribed to $CuMnO_2$ with (-2 0 1) and (-1 1 1) exposed crystal facets were identified. Moreover, additional facets related to the $CuMn_2O_4$ crystalline phase were also detected, with interplanar distances of 0.188 nm (3 3 1), 0.238 nm (2 2 2), and 0.250 nm (3 1 1). These results may suggest a more complex internal structure, due to the coexistence of both identified phases, whose schematic representation is given in Fig. 3. The same crystalline phases were observed for the remaining two copper-containing samples; however, simultaneous additional facets were also detected. The main differences observed in TEM images were related to the crystallinity of the structures. Indeed, both $CuMnO_x$_SCS and $CuMnO_x$_oxalate exhibited more crystalline areas, which were well distinguishable from the amorphous ones, above all for the oxalate sample. This was also consistent with the results of XRD analyses. The coexistence of multiple crystalline phases within the same structure (as observed in Fig. 3) may locally generate lattice strain at the phase boundaries. Thus, the interface between these phases can induce structural defects, which are known in the literature to favor enhanced oxygen mobility and catalytic activity in mixed oxide systems [17,46,47].

STEM-EDX maps were collected to confirm the presence and distribution of copper within the studied binary structures. As shown in Fig. 4, copper was found to be homogeneously distributed in the manganese oxide matrix, with no segregation detected for both $CuMnO_x$_redox and $CuMnO_x$_SCS samples. This indicated that copper was well stabilized within the studied structures without forming larger oxoclusters or separate phases. This effect was also confirmed by structural analyses (XRD and RS). On the other hand, in the case of the $CuMnO_x$_oxalate sample, it was possible to observe areas of different content of copper, indicating that this synthesis procedure was not able to homogeneously incorporate copper in the manganese oxide matrix.

To further investigate the homogeneity of the studied material, several EDX spectra were acquired from several morphologically different regions. In the case of the $CuMnO_x$_redox catalyst, the results confirmed that the sample is highly homogeneous, with about 9.3 wt% total copper content in the entire copper-manganese oxide material. This value corresponds to a Cu/(Cu+Mn) mass ratio of approximately 13.7 wt%, in line with the synthesis procedure (i.e., 15 wt%). A small amount of K was also detected (see Table S2) due to residuals from the synthesis procedure, as also reported by other authors. However, it is expected to have a negligible impact on the properties or performance of the material. The SCS sample was less homogeneous compared to the

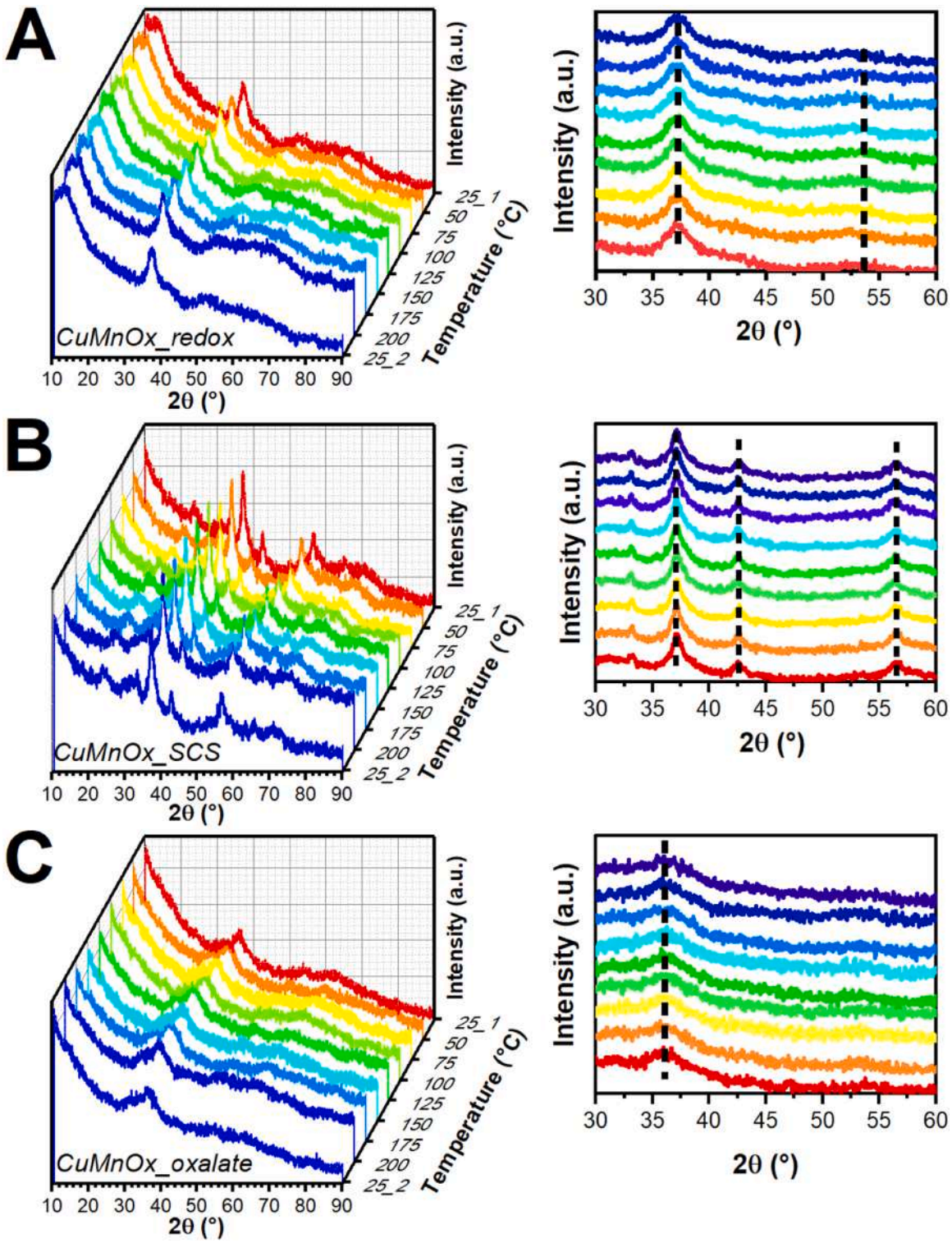

Fig. 2. Variable-temperature XRD patterns of $CuMnO_x$_redox (A), $CuMnO_x$_SCS (B), and $CuMnO_x$_oxalate (C), collected under air atmosphere at different temperatures in the range 25–200 °C.

previous one; however, a good distribution of copper was reached with a Cu/(Cu+Mn) mass ratio of approximately 17.0 wt%. Finally, the oxalate sample highlighted the worst distribution with a Cu/(Cu+Mn) mass ratio of 11.3 wt%.

The elemental composition and the oxidation state of the surface species of the catalysts (namely, Mn, O, and Cu elements) were investigated through XPS measurements. The results related to the relative amounts of the detected component species were reported in Figure S5 and summarized in Table 3, whereas O 1s, Mn 3s, and Cu 2p XPS deconvoluted spectra were reported in Fig. 5.

Figure S6 displays the Mn 2p core level spectra. Specifically, the peak at c.a. 641.8–642.2 eV binding energy (BE) was related to Mn $2p_{3/2}$, whereas the peak at higher BE (c.a. 653.6–654.1 eV) corresponds to the Mn $2p_{1/2}$ peak [48]. The relative abundance of the Mn species (i.e., Mn^{4+} and Mn^{3+}) can be evaluated from the deconvolution of the band recorded in the Mn $2p_{3/2}$ window. Precisely, all the samples showed two

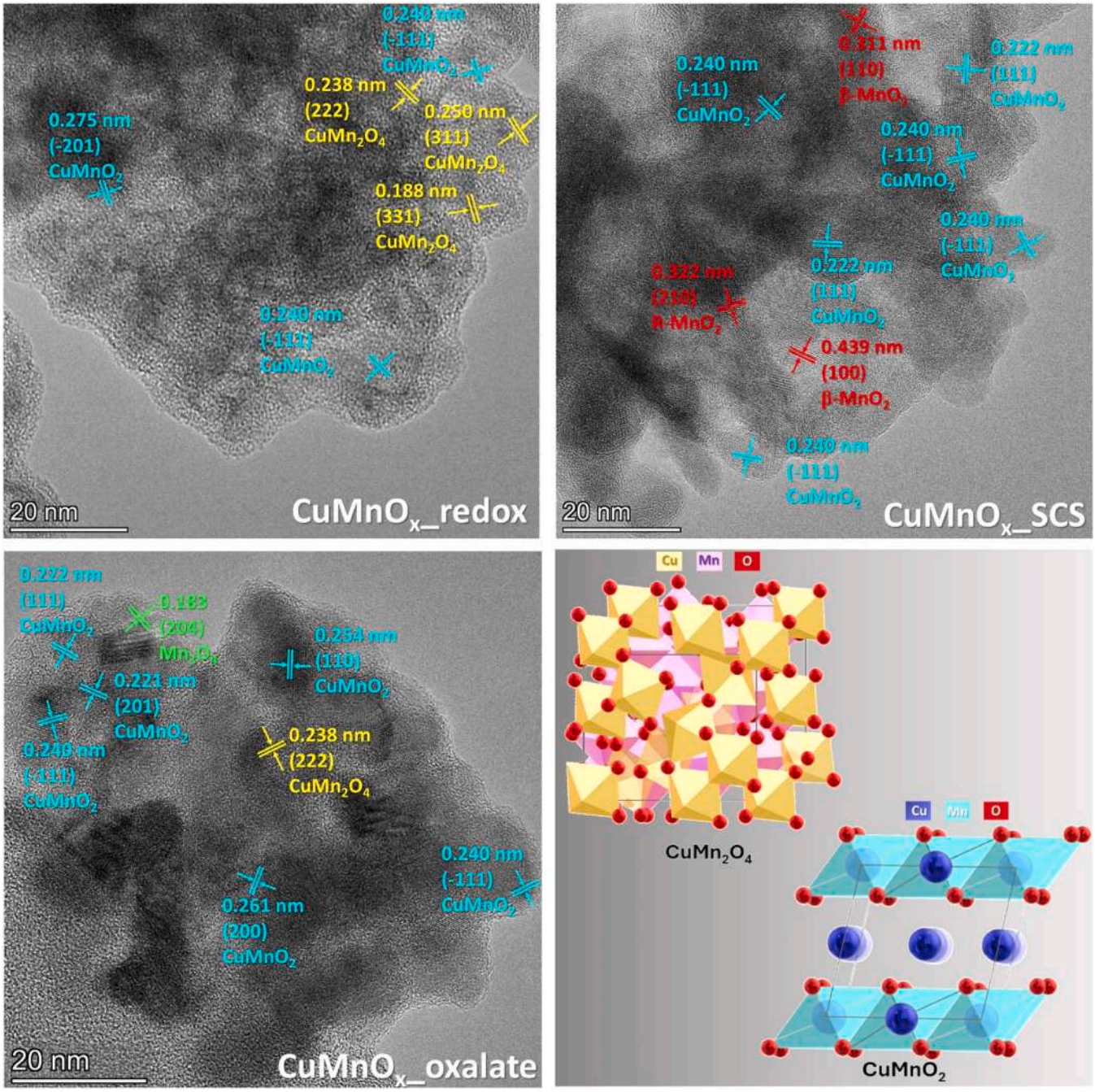

Fig. 3. HR-TEM images of $CuMnO_x$_redox, $CuMnO_x$_SCS, and $CuMnO_x$_oxalate samples, with their respective crystalline phases identified and a schematic representation of the possible crystalline structures characteristic of the $CuMnO_x$ binary system.

characteristic peaks: the former in the range of 641.7–642.2 eV can be ascribed to Mn^{3+} species, and the latter at 643.1–643.7 eV can be related to Mn^{4+} species [27,48–53].

Moreover, the elaboration of the band recorded in the Mn 3s orbital (see Fig. 5**A**) confirmed that the sample obtained via the oxalate route exhibited a lower average oxidation state (AOS), and, consequently, a higher amount of Mn^{3+} species, as reported in Table 3. This was consistent with the results obtained from the XRD analysis and TPR (see below).

By introducing copper to the MnO_x structures, a slight decrease in the AOS was observed compared to the pure manganese oxides; however, the same trend in AOS values was maintained (SCS > redox > oxalate). This decrease could be related to the effective stabilization of copper centers within the manganese oxide structure, which favored the redox couple Cu^{2+}-Mn^{3+} instead of Cu^{+}-Mn^{4+}. The predominant presence of Cu^{2+} was confirmed from the elaboration of the copper spectrum and Cu LMM (see below).

Fig. 5**B** shows the O 1s core levels. As highlighted by the deconvolution, different oxygen species were detected. The first peak in the range of 529.4–529.8 eV can be ascribed to bulk oxygen O_β (O^{2-} species) [46,48,52], and, not surprisingly, this is the major component (see Figure S5). The second one was located at 531.1–531.7 eV, and it was ascribed to superficial reactive oxygens, labeled as O_α (i.e., O_2^-, O^-, OH^-), and to oxygen vacancies, as previously observed in other works [17,48,51,52,54,55]. Moreover, in all the samples, except for MnO_x_SCS, a further peak at 532.6–533.4 eV was detected, labeled as O_γ, and attributed to adsorbed oxygen, surface adsorbed carbonate, and hydroxyl species, probably due to chemisorption of water [54–58].

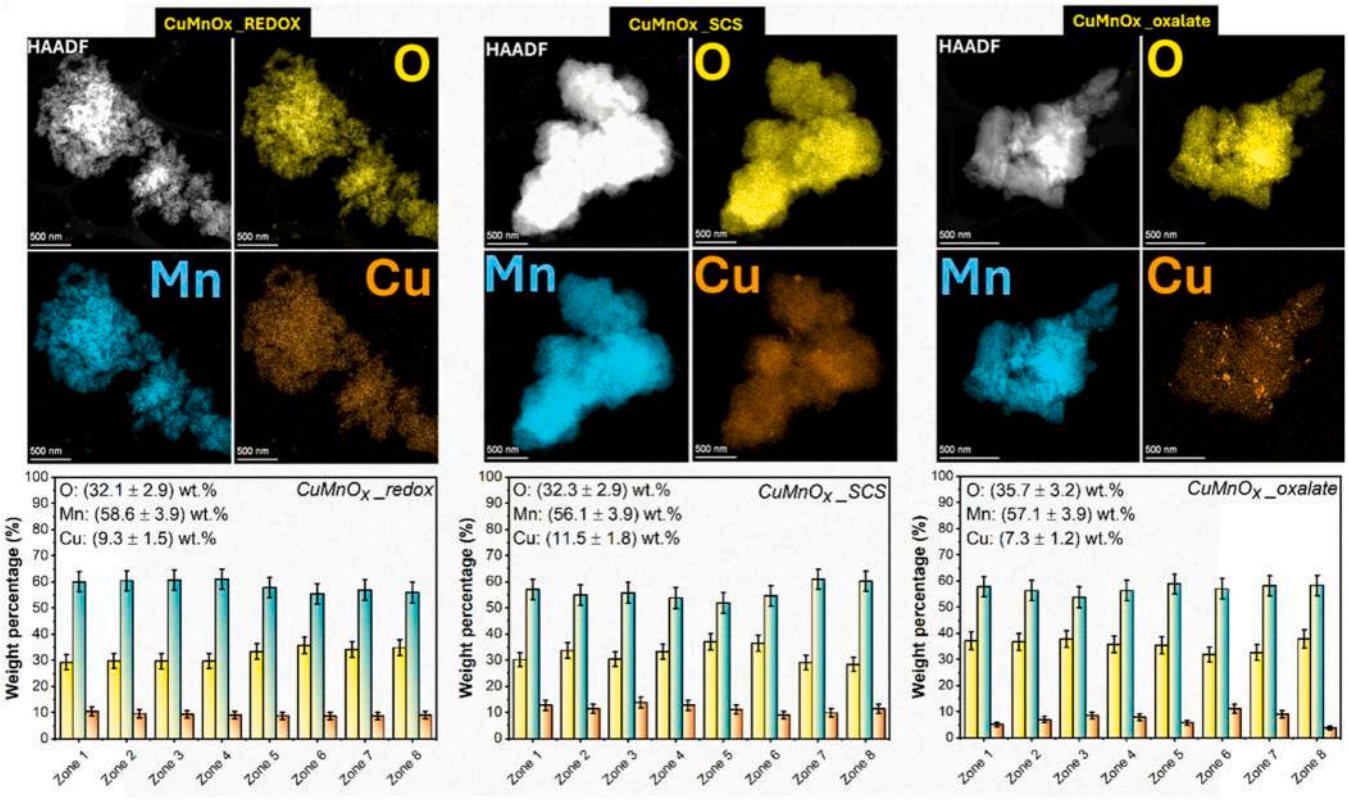

Fig. 4. STEM-EDX maps and elemental quantification of $CuMnO_x$ samples.

Table 3
Average oxidation state (AOS) evaluated from Mn 3s spectrum and relative abundance of the species evaluated from the deconvolution of O1s and Cu 2p XPS spectra.

Sample	AOS[a] (-)	$(O_\alpha+O_\gamma)/O_\beta$ (-)	Cu^{2+} (%)
$CuMnO_x$_SCS	3.5	0.75	98.08
$CuMnO_x$_oxalate	3.2	0.83	99.06
$CuMnO_x$_redox	3.4	1.04	99.95
MnO_x_SCS	3.7	0.64	
MnO_x_oxalate	3.1	0.68	
MnO_x_redox	3.7	0.61	

[a] AOS = 8.95–1.13 × ΔE_s, where the ΔE_s is the splitting energy of the Mn 3 s

Surface reactive oxygen species (O_α) can play a pivotal role in catalytic oxidation [46,56]. An increase in surface-active oxygen content may be beneficial to the transfer of reactive oxygen species from the catalyst surface to the pollutant molecules, thus promoting their oxidation [56]. The ratio of O_α/O_β is also an informative parameter to estimate the relative abundance of oxygen vacancies occurring in the catalysts. The more oxygen species adsorbed on the surface, the higher the oxygen vacancy density [59]. Based on these premises, the $CuMnO_x$_redox sample exhibited the highest percentage of reactive oxygen (46.7 %) compared to $CuMnO_x$_SCS and $CuMnO_x$_oxalate (40.4 % and 41.6 %, respectively). Moreover, the presence of copper greatly increased the concentration of O_α species, especially for the $CuMnO_x$_redox sample. This is consistent with the fact that the introduction of copper increases the mobility of surface oxygen species, as revealed in the literature. This outcome may suggest an enhancement of the activity toward the VOCs oxidation reaction since O_α species have higher mobility than lattice oxygen O_β [46].

Finally, Fig. 5**C** reports the Cu 2p spectra for the Cu-containing samples. The presence of shake-up satellite peaks was related to the presence of Cu^{2+} in all studied $CuMnO_x$ catalysts. Many works [60,61] reported the results of deconvolution of Cu 2p spectrum, but they may not be reliable enough due to the overlapping of the spectral contributions from different Cu oxidation state binding energies, making the deconvolution complex. Therefore, the amounts of Cu^{2+} and $Cu^0 + Cu^{1+}$ were estimated by fitting the Cu $2p_{3/2}$ peak and its related satellite, as reported elsewhere [62–64]. The results in Table 3 revealed that Cu^{2+} is the predominant species in the near-surface region of the catalysts. Precisely, the $CuMnO_x$_redox sample exhibited 99.9 % of Cu^{2+} species, followed by the corresponding contents determined for $CuMnO_x$_oxalate and $CuMnO_x$_SCS samples with 99.1 % and 98.1 % of Cu^{2+} contents, respectively. Moreover, the Cu LMM peak shape can also be useful in determining Cu chemical states [65,66]. In all three cases, when plotting the spectrum as a function of kinetic energy, a peak at 917.6 eV is clearly observed. This peak is characteristic of CuO, along with the corresponding shape typical for this compound. Furthermore, the deconvolution of the Cu LMM (Fig. 5**D**), as reported in the literature [65], revealed results that were in close agreement with those obtained by fitting the Cu $2p_{3/2}$ spectrum. The deconvolution process allows for a more detailed analysis of the different copper species present in the samples. In this context, it was also possible to distinguish the relative percentages of different Cu^{2+} species, specifically CuO and $Cu(OH)_2$. The results showed that CuO was predominant in all cases, with percentages of 64.5 % in the $CuMnO_x$_SCS sample, 77.6 % in the $CuMnO_x$_oxalate sample, and 64.4 % in the $CuMnO_x$_redox sample. On the other hand, the $Cu(OH)_2$ species was present at 33.6 % in the $CuMnO_x$_SCS sample, 21.5 % in the $CuMnO_x$_oxalate sample, and 35.6 % in the $CuMnO_x$_redox sample. The remaining fractions were related to $Cu^0 + Cu^{1+}$. These values provided a detailed understanding of the copper species distribution in each sample, highlighting the effect of different synthesis procedures on the copper oxidation states.

Figure S7 shows the H_2-TPR profiles as a function of the temperature, whereas Table 4 reports the H_2 uptakes for all the catalysts investigated. Pure MnO_x samples showed reduction peaks at lower temperatures, compared to the literature [52,67,68], indicating a higher tendency of

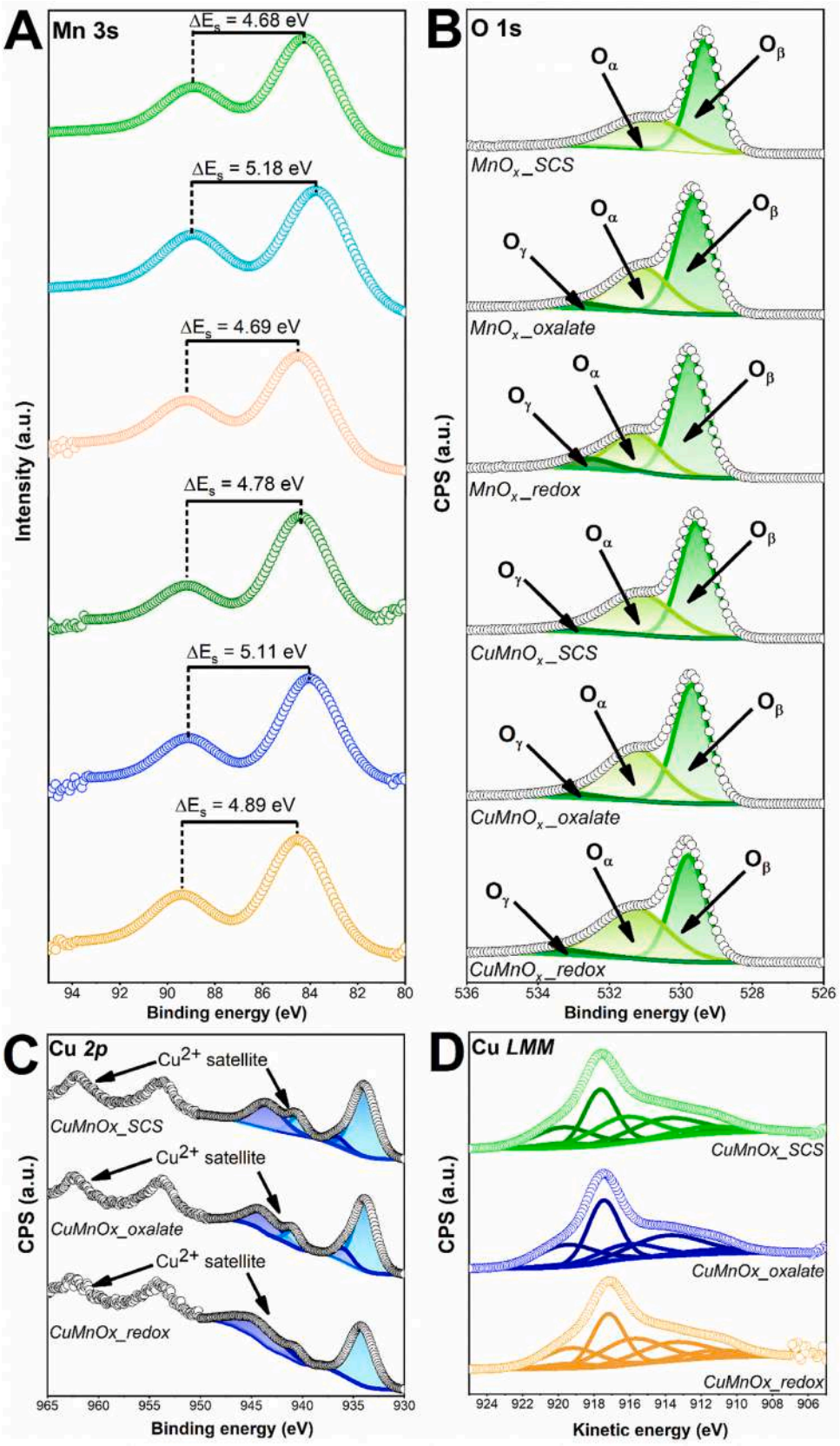

Fig. 5. XPS spectra of Mn 3s (A), O 1s (B), Cu 2p (C), and Cu LMM (D) for the prepared samples.

Table 4
Total and partial H_2-uptake per unit of catalyst and for each single maximum evaluated from TPR profiles.

Sample	Total H_2 uptake (mmol g_{cat}^{-1})	H_2-uptake 50 - 200 °C (mmol g_{cat}^{-1})	H_2-uptake 200 °C - 400 °C (mmol g_{cat}^{-1})	H_2-uptake > 400 °C (mmol g_{cat}^{-1})
$CuMnO_x$_SCS	15.12	2.85	11.61	0.66
$CuMnO_x$_oxalate	9.16	3.21	5.17	0.78
$CuMnO_x$_redox	11.34	4.34	5.67	1.33
MnO_x_SCS	11.78	0.23	9.52	2.03
MnO_x_oxalate	7.67	0.78	6.62	0.27
MnO_x_redox	11.00	1.34	8.81	0.85

the studied catalysts to reduce. This higher reducibility is associated with higher mobility of oxygen species [69], as also confirmed by O_2-TPD analysis (see below).

Depending on the valence state of Mn species, different reduction profiles can be observed. For all the undoped manganese oxide samples, the shoulder at low temperature (at ca. 200 °C) could be related to the release of reactive oxygen species from the surface [17,46,70]. Thus, it would be possible to correlate the catalytic activity of pollutant oxidation with oxygen mobility [71]. For the MnO_x_SCS sample, the maxima centered at 311 °C and 412 °C could be ascribed to the reduction of $MnO_2 \rightarrow Mn_2O_3$ or of $Mn_2O_3 \rightarrow Mn_3O_4$ for the former peak, and the formation of MnO for the latter one [72,73]. This was also consistent with our previous work [17]. A similar profile was obtained for the MnO_x_oxalate sample, for which the positions of the H_2 consumption peaks shifted to lower temperatures compared to those characteristic of the TPR profile recorded for the MnO_x_SCS sample. The presence of two peaks could be explained by taking into consideration the structure of nonstoichiometric Mn_3O_4. As reported in the literature [71,74], three kinds of Mn^{3+}-O bonds can be distinguished in the coordination polyhedron typical of this oxide. They are classified as octahedral long Mn^{3+}-O, octahedral short Mn^{3+}-O, and tetrahedral Mn^{3+}-O. Obviously, the stronger the bond, the higher the corresponding reduction temperature. Based on these premises, the first reduction peak at 249 °C could be related to the Mn^{3+} ions in tetrahedral coordination or Mn^{3+} in elongated octahedra, whereas the second one at 382 °C can be assigned to the co-reduction of the above-mentioned structures containing Mn^{3+} ions in shortened octahedra [71].

Finally, the MnO_x_redox sample had a different reduction profile compared to the previous samples. Specifically, it exhibited the main reduction peak in the region ranging from 200 to 350 °C, with the presence of two different shoulders, whereas the peak at higher temperatures (ca. 427 °C) presented extremely low intensity compared to the former. This could mean that the reduction process takes place in the region up to 350 °C, where the simultaneous transformation of $MnO_2 \rightarrow Mn_2O_3 \rightarrow Mn_3O_4 \rightarrow MnO$ can occur. Most probably, the peak at higher temperatures was related to the bulk reduction to MnO.

Focusing on the copper-containing samples, it appeared quite clear that the presence of copper enhanced the reducibility of the bare manganese oxides, shifting the reduction peaks in the corresponding TPR profiles to lower temperatures in all analyzed cases. This could be related to an increase in oxygen mobility due to the interaction between Cu and Mn within the binary system [75,76]. In fact, by comparing the copper-containing catalysts with their counterparts (see panels a1, a2, and a3 in Figure S7), an increase in the reducibility was observed, both in terms of hydrogen consumption (Table 4) and peak shift at lower temperatures. The Cu-containing samples presented asymmetric reduction peaks, as also reported in the literature [77,78]. The shoulders at lower temperatures (134 °C for $CuMnO_x$_redox sample, 157 °C for $CuMnO_x$_oxalate sample, and 206 °C for $CuMnO_x$_SCS sample, as revealed after the deconvolution) could be ascribed to the reduction of Cu^{2+} to Cu^0, and the maxima positions were significantly lower than those reported in the literature [45,77]. This implies that the interactions between Cu and Mn species improved the overall reducibility. The other peaks could be attributed to the stepwise reduction of $MnO_2 \rightarrow Mn_2O_3 \rightarrow Mn_3O_4 \rightarrow MnO$. The comparison of the H_2 consumption between copper-free and copper-containing samples revealed some interesting trends. Based on the calculated H_2 consumption, obtained by integrating the area under the curve of the TPR profile, it was evident that the MnO_x_SCS sample exhibited the highest H_2 consumption (11.78 mmol g^{-1}), followed by those determined for MnO_x_redox and MnO_x_oxalate samples (11.0 and 7.67 mmol g^{-1}, respectively). This trend was consistent with the average oxidation state from XPS: samples with a higher fraction of Mn^{3+} species, indicating a lower oxidation state, showed lower H_2 consumption. However, it should be noted that TPR measures bulk reducibility, while XPS probes surface oxidation states; therefore, this comparison is intended as a qualitative observation rather than a direct quantitative correlation. Based on this, the MnO_x_oxalate sample, with a lower oxidation state (3.1) and a higher concentration of Mn^{3+} species, showed lower H_2 uptake compared to that determined for MnO_x_SCS and MnO_x_redox samples. Focusing on the latter two samples, despite having the same AOS, the two catalysts evidenced slightly different H_2 consumption, higher in the case of the SCS sample than in the case of the MnO_x_redox one. However, when examining H_2 uptake at low temperatures, the redox sample demonstrated a higher uptake (1.34 mmol g^{-1}) between 50 and 200 °C, compared to MnO_x_SCS and MnO_x_oxalate catalysts, which only reached 0.23 and 0.78 mmol g^{-1}, respectively, in the same temperature range. This could have significant implications for catalytic performance, as higher H_2 consumption at lower temperatures suggests greater oxygen mobility and may potentially enhance catalytic performance even at lower temperatures.

When comparing the copper-containing samples with their copper-free counterparts, it was evident that the presence of copper increased hydrogen consumption. This could be attributed to the fact that, in addition to manganese, copper also requires H_2 for its reduction. Furthermore, as previously mentioned, copper incorporation in the structure increased the amount of mobile oxygen species in the bulk, which can diffuse to the surface and enhance oxygen mobility. On the surface, this results in a higher concentration of reactive oxygen species, contributing to improved catalytic activity. The higher H_2 uptake in the $CuMnO_x$_SCS sample compared to the $CuMnO_x$_redox sample may be explained by considering the AOS values. Specifically, for the $CuMnO_x$_redox samples, the AOS shifted from 3.7 to 3.4, indicating that the copper presence altered the oxidation state of manganese, increasing Mn^{3+} species (see Table 3). However, simultaneously, the content of Cu^{2+} species also increased, leading to an overall higher H_2 consumption compared to the copper-free MnO_x sample. A similar reasoning applies to the $CuMnO_x$_SCS sample, which exhibited much higher hydrogen consumption than the $CuMnO_x$_redox catalyst. This is because, even if $CuMnO_x$_SCS contained a slightly lower percentage of Cu^{2+}, it had a higher concentration of Mn^{4+} species than $CuMnO_x$_redox catalyst, which may explain the greater H_2 consumption in the former sample. However, focusing on the uptake at lower temperatures, $CuMnO_x$_redox exhibited the highest H_2 consumption among all the samples investigated. Specifically, it was observed to be 3.2 times higher than its copper-free counterpart and 1.5 times greater than that of the $CuMnO_x$_SCS catalyst, which instead showed the highest consumption at medium-high temperatures (200–400 °C). This may suggest that the presence of copper in the $CuMnO_x$_redox sample enhances hydrogen uptake at lower temperatures, likely due to the increased mobility of oxygen species, which can have a significant impact on catalytic performance in the corresponding temperature range.

The oxygen mobility and the associated capacity of the materials investigated to provide reactive oxygen species were investigated through O_2-TPD. The corresponding profiles are illustrated in Fig. 6, whereas the amount of oxygen desorbed from individual samples was summarized in Table 5.

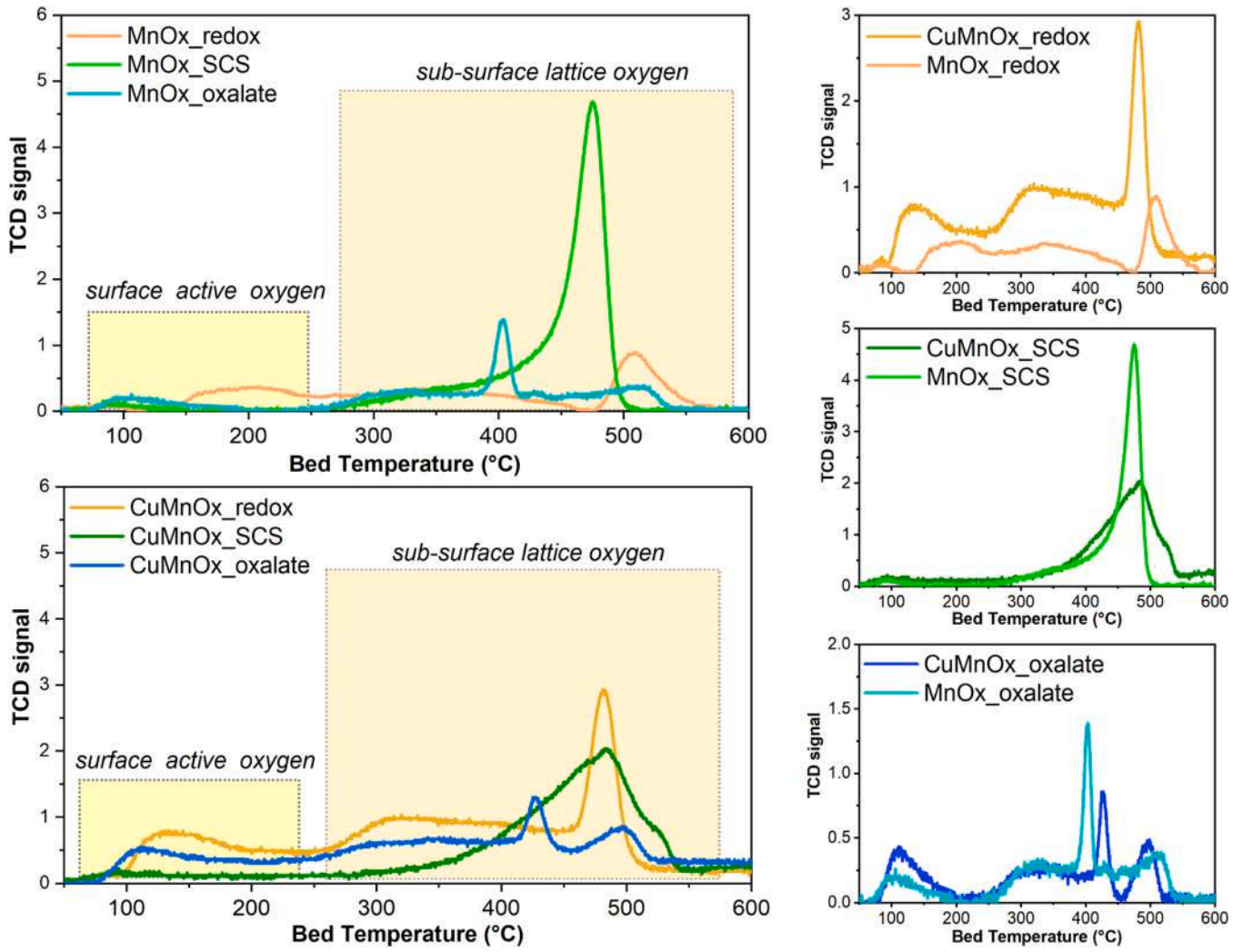

Fig. 6. O_2-TPD profiles as a function of the temperature of pure MnO_x and copper-containing samples and their respective comparison (panels on the right).

Table 5
Total and partial O_2-desorption per mass unit of catalyst and for each single peak evaluated from O_2-TPD profiles.

Sample	Total O_2 uptake (mmol g_{cat}^{-1})	O_2-uptake 50 - 250 °C (mmol g_{cat}^{-1})	O_2-uptake 250 °C - 600 °C (mmol g_{cat}^{-1})
$CuMnO_x$_SCS	10.38	0.89	9.49
$CuMnO_x$_oxalate	4.69	1.19	3.50
$CuMnO_x$_redox	14.28	3.44	10.84
MnO_x_SCS	8.89	0.23	8.66
MnO_x_oxalate	4.29	0.83	3.45
MnO_x_redox	4.87	1.35	3.52

The O_2-TPD profiles, obtained for all the investigated samples, revealed the desorption of different oxygen species in terms of nature and amount, highlighting significant differences in oxygen mobility depending on the synthesis procedure adopted. Within the low-temperature range of 50–250 °C, the desorption peaks were primarily associated with surface reactive oxygen species, which may play a pivotal role in catalytic oxidation processes at low temperatures. The release of oxygen in this temperature range indicated a rather weak metal-oxygen interaction. This was accentuated in copper-containing samples (especially for $CuMnO_x$_redox and $CuMnO_x$_oxalate) due to the substitution of aliovalent Mn centers with Cu^{2+}. This substitution led to the formation of oxygen vacancies and enhanced oxygen mobility. To describe the defect chemistry upon Cu^{2+} substitution of Mn^{4+} into the MnO_2 lattice, Kröger–Vink notation was used, and the possible reaction was written as follows:

$$Cu^{2+} + Mn_{Mn}^{x} + O_O^{x} \rightarrow \quad a) \quad Cu_{Mn}'' + 2Mn_{Mn}' + 2V_{\ddot{O}}$$
$$b) \quad Cu_{Mn}'' + V$$

where Cu^{2+} replaces Mn^{4+} (Cu_{Mn}''), generating Mn^{3+} (Mn_{Mn}') species and oxygen vacancies ($V_{\ddot{O}}$) to preserve charge neutrality. These oxygen-defect structures are essential for promoting oxygen mobility and facilitating oxidation of pollutants from the gas phase [79].

In contrast, the oxygen desorption peaks observed at intermediate temperatures, i.e., between 250 °C and 600 °C, corresponded mainly to sub-surface lattice oxygen species, reflecting oxygen more strongly stabilized within the bulk structure and less directly involved in surface reactions.

It was noteworthy to observe that both pure MnO_x and copper-containing samples synthesized via the redox and oxalate routes exhibited well-visible low-temperature oxygen desorption maxima attributable to highly reactive oxygen species. On the other hand, these maxima were almost absent in the profiles recorded for samples prepared by the SCS method. In fact, quantitative integration of the desorption profiles revealed that the amount of oxygen released at low temperatures from the SCS samples was negligible, specifically, 0.23 mmol g^{-1} and 0.89 mmol g^{-1} for MnO_x_SCS and $CuMnO_x$_SCS, respectively, as detailed in Table 5. This finding clearly indicates

significantly reduced oxygen mobility in the catalysts prepared via the SCS route compared to their redox- and oxalate-derived counterparts. Therefore, the overall trend for low-temperature oxygen desorption can be summarized as follows: $CuMnO_x$_redox > $CuMnO_x$_oxalate > $CuMnO_x$_SCS.

$CuMnO_x$_redox sample was particularly noteworthy since it exhibited remarkably high oxygen desorption at low temperatures, exceeding values commonly reported in the literature [80,81]. The oxygen released from this sample at low temperature is 2.9 times greater than that determined in the case of the Cu-oxalate sample and 3.9 times higher than that determined for the Cu-SCS sample. This could imply superior catalytic activity, especially for the oxidation of indoor air pollutants. Moreover, this redox sample demonstrated the highest total oxygen desorption over the entire temperature range, which was equal to 14.28 mmol g^{-1}.

In contrast, $CuMnO_x$_oxalate exhibited the lowest value, 4.69 mmol g^{-1}, which was 2.2 times lower than that determined for $CuMnO_x$_SCS. In fact, considering the total oxygen desorbed, the SCS samples seemed to exhibit high mobility. However, it is crucial to focus attention on the desorption in a specific, low-temperature range. In fact, both samples prepared via the SCS technique predominantly released oxygen at higher temperatures in comparison to the other samples studied. This behavior suggested that lattice oxygen in these catalysts was more stable at low temperatures but became active at elevated temperatures. This observation implied that their optimal catalytic performance may occur in medium-to-high temperature regimes rather than in low-temperature conditions.

The NH_3-TPD analysis of the three $CuMnO_x$ binary oxide catalysts was carried out to investigate the acidity of the samples, which can play an important role in oxidation reactions. The results are reported in Figure S8 and in Table 6, revealing variations in both the total acidity and the distribution of acid sites across different temperature ranges, depending on the synthesis methods. The $CuMnO_x$_redox sample exhibited the highest overall acidity with a total NH_3 desorption amount of 3.25 mmol g^{-1}, distributed among weak Brønsted acid sites (1.06 mmol g^{-1} desorbed between 100 and 250 °C), medium acid sites (1.16 mmol g^{-1} desorbed between 250 and 450 °C), and strong Lewis acid sites (1.03 mmol g^{-1} desorbed above 450 °C). This balanced presence of acid sites across the entire temperature spectrum suggested a diverse acid environment, which is often beneficial for catalytic processes requiring different acid strengths. In contrast, the $CuMnO_x$_SCS catalyst demonstrated a different acid profile, characterized by a predominance of strong acid sites with 1.74 mmol g^{-1} desorbed above 450 °C, while exhibiting very limited weak acidity (only 0.06 mmol g^{-1} in the 100 - 250 °C range) and moderate medium acid sites (1.00 mmol g^{-1}). Finally, the $CuMnO_x$_oxalate sample exhibited the lowest total acidity of 1.46 mmol g^{-1}, with a considerable fraction of weak acid sites (0.42 mmol g^{-1}) and medium acid sites (0.76 mmol g^{-1}), but a notably small amount of strong acid sites (0.28 mmol g^{-1}). These pronounced differences in both the quantity and strength of acid sites highlighted how the synthesis route strongly impacted the acid properties of $CuMnO_x$ catalysts, which in turn were expected to affect their catalytic performance in oxidation reactions.

Table 6
Total and partial NH_3-desorption per mass unit of catalyst and for each single peak evaluated from NH_3-TPD profiles.

Sample	Total NH_3 desorption (mmol g_{cat}^{-1})	NH_3 desorption 100–250 °C (mmol g_{cat}^{-1})	NH_3 desorption 250 °C - 450 °C (mmol g_{cat}^{-1})	NH_3 desorption >450 °C (mmol g_{cat}^{-1})
$CuMnO_x$_SCS	2.80	0.06	1.00	1.74
$CuMnO_x$_oxalate	1.46	0.42	0.76	0.28
$CuMnO_x$_redox	3.25	1.06	1.16	1.03

3.2. Catalytic activity and stability test

The CO oxidation catalytic test results are presented in Fig. 7. As revealed by the comparison of catalysts synthesized using the same technique, the presence of copper in the structure significantly enhanced the catalytic performance for CO oxidation, as also shown in Table 7. Among the pure manganese oxide samples, the one synthesized via the redox technique was the most effective: it indeed reached a reaction rate of 13.9 μmol $h^{-1}g^{-1}$ (Table 8) at RT and completely oxidized CO at 75 °C. When comparing the undoped catalysts with the Cu-containing samples, a decrease in the temperature at which the pollutant was completely converted to CO_2 was observed, clearly highlighting the beneficial effect of copper on catalytic activity. Among the copper-containing catalysts, the most effective were $CuMnO_x$_redox and $CuMnO_x$_oxalate, both achieving complete CO conversion at room temperature. At the same temperature, the $CuMnO_x$_SCS sample converted 60 % of the CO.

In all cases, the catalysts showed exceptionally high performance, successfully oxidizing the pollutant without the use of noble metals (e.g., Au or Pt), highlighting their promising potential for indoor air purification applications. Given the outstanding results obtained via redox and oxalate routes, these catalysts were further tested by performing TOS (time-on-stream) evaluations to assess their stability. The results are shown in Figure S9. Both $CuMnO_x$_redox and $CuMnO_x$_oxalate samples demonstrated excellent stability, maintaining full conversion for at least 6 consecutive hours. However, $CuMnO_x$_oxalate catalyst exhibited a slight decrease after 2 h, in contrast to the catalytic performance shown by $CuMnO_x$_redox sample, whose activity remained unaltered over time. This indicated that the catalyst was able to operate for prolonged periods under the reaction conditions, maintaining its catalytic performance unchanged, thus reflecting strong structural stability and reproducibility over time. Moreover, since the $CuMnO_x$_redox sample exhibited the highest catalytic activity and stability, an extended TOS test was performed over a duration of 250 h for the CO reaction. The results, shown in Fig. 7, demonstrated that the catalyst maintained exceptionally high catalytic activity throughout the entire testing period under the reactive gas mixture. Remarkably, a CO conversion of 93 % was achieved after 250 h of continuous operation, resulting in a conversion loss of 6.8 %, highlighting both the outstanding performance and long-term stability of the material.

The conversion curves and TOS analysis for the catalytic oxidation of ethylene are reported in Fig. 8 and Figure S10. Since the bond energy of C-H bonds (413 kJ mol^{-1}) and C═C bonds (615 kJ mol^{-1}) is higher than that of C═O in carbon monoxide, ethylene oxidation is more difficult [82]. As shown in Fig. 8, the introduction of copper into the catalyst structure significantly improved the overall catalytic activity of all the samples. In particular, the $CuMnO_x$_redox catalyst exhibited catalytic activity at temperatures as low as 75 °C, demonstrating T_{10}, T_{50}, and T_{90} values at 85 °C, 118 °C, and 146 °C, respectively. These values are much lower compared to those of the other samples, as shown in Table 7. For the same sample, the conversion rate evaluated at 100 °C was 44 μmol h^{-1} g^{-1}, which was higher than that of $CuMnO_x$_oxalate (20 μmol h^{-1} g^{-1}) and $CuMnO_x$_SCS (15.5 μmol h^{-1} g^{-1}), as illustrated in Table 8. This indicated a remarkable improvement in performance, not only due to the addition of copper, which enhanced the catalytic properties compared to the undoped manganese oxide, but also due to the optimization of the synthesis procedure. This result highlighted that, while both the $CuMnO_x$_redox and $CuMnO_x$_oxalate samples showed exceptional CO oxidation performance at around 20 °C, differences in activity were more evident in the case of ethylene, with $CuMnO_x$_redox emerging as the most effective catalyst.

Moreover, since moisture is usually present in indoor environments, oxidation tests toward CO and ethylene were also carried out in the presence of polluted air fully saturated with moisture at 25 °C, which corresponds to the situation that is the most demanding for catalytic performance. Catalytic oxidation tests under wet conditions were

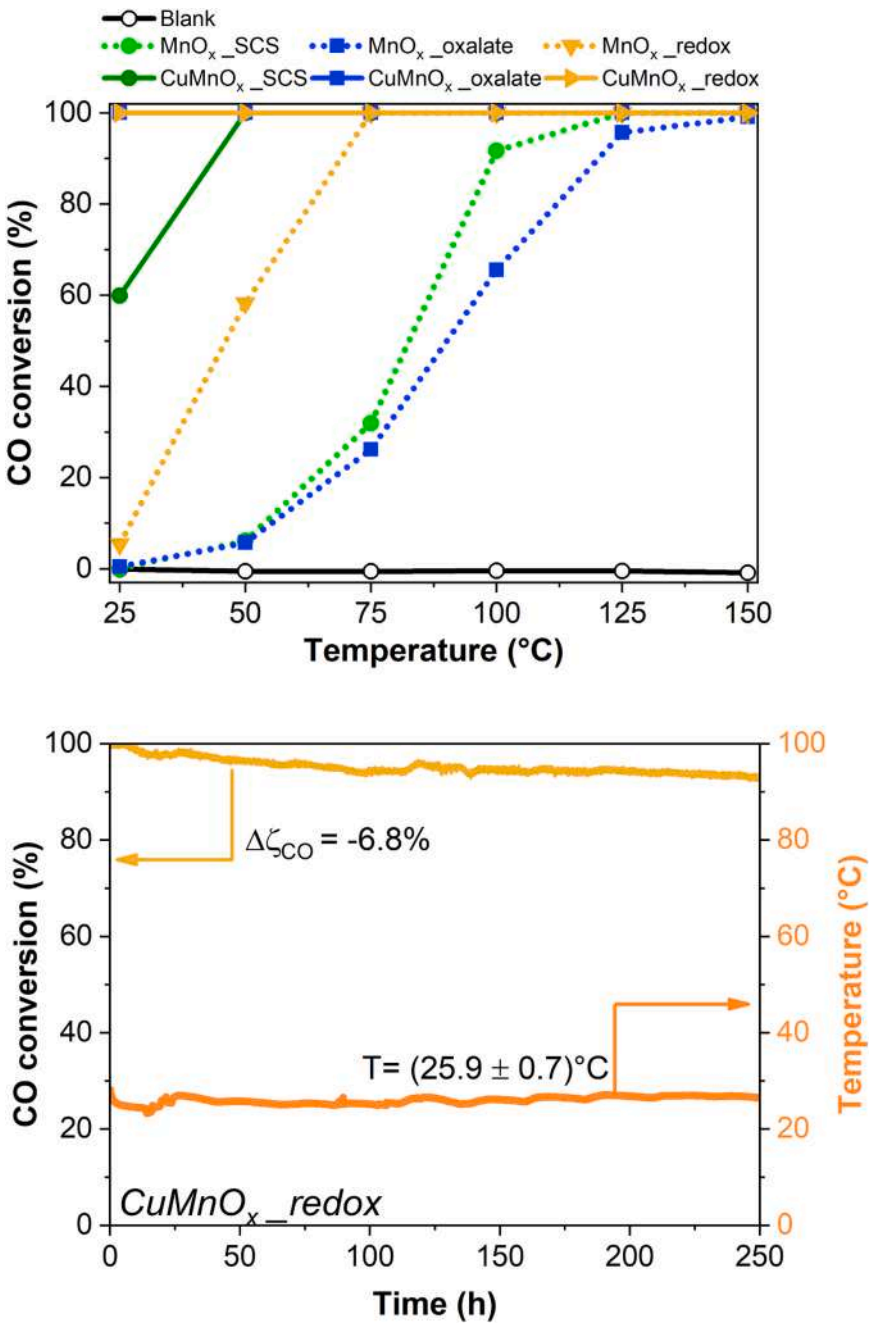

Fig. 7. Catalytic conversion of CO as a function of the temperature in dry conditions, and Time-On-Stream (TOS) analysis performed at isothermal condition T_{100}, by feeding a gaseous mixture with 100 ppm of CO, 21 vol% O_2, and N_2 to balance over 50 mg of catalyst.

Table 7
Values of T_{10}, T_{50}, and T_{90} evaluated for CO and ethylene oxidation over the catalysts.

Sample	CO			Ethylene		
	T_{10} (°C)	T_{50} (°C)	T_{90} (°C)	T_{10} (°C)	T_{50} (°C)	T_{90} (°C)
MnO_x_SCS	54	83	99	119	169	209
$CuMnO_x$_SCS	< RT	< RT	44	104	139	175
MnO_x_oxalate	55	90	120	105	147	170
$CuMnO_x$_oxalate	< RT	< RT	< RT	101	130	156
MnO_x_redox	27	46	69	92	130	161
$CuMnO_x$_redox	< RT	< RT	< RT	85	118	146

RT: room temperature ≈ 19–20 °C

Table 8
Conversion rates evaluated for CO and ethylene oxidation over catalysts.

Sample	CO[a]		Ethylene[b]	
	μmol h^{-1} g^{-1}	μmol h^{-1} m^{-2}	μmol h^{-1} g^{-1}	μmol h^{-1} m^{-2}
MnO_x_SCS	no activity	no activity	8.9	0.250
$CuMnO_x$_SCS	194.6[c]	4.324[c]	15.5	0.342
MnO_x_oxalate	1.5	0.008	16.1	0.088
$CuMnO_x$_oxalate	140.8[c]	0.395[c]	20.0	0.056
MnO_x_redox	13.9	0.056	37.6	0.152
$CuMnO_x$_redox	494.3[c]	1.502[c]	44.0	0.134

[a] rate evaluated at RT
[b] rate evaluated at 100 °C
[c] rate evaluated performing tests with 10 mg of catalyst instead of 50 mg

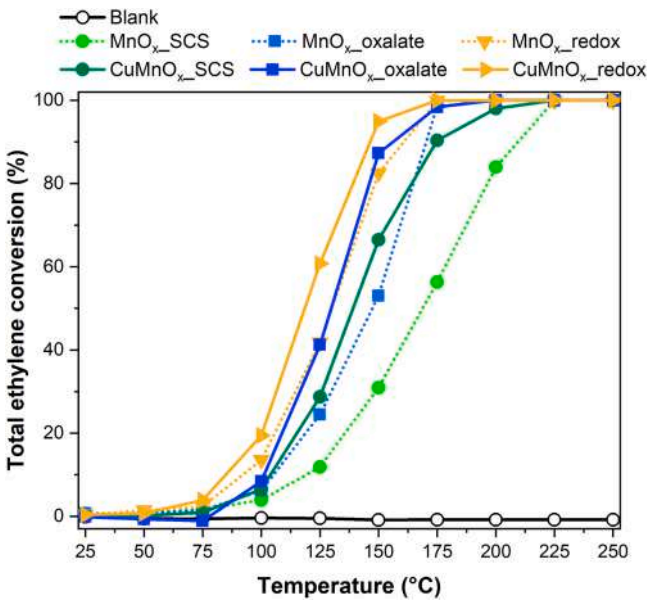

Fig. 8. Catalytic conversion of ethylene as a function of the temperature in dry conditions performed by feeding a gaseous mixture with 100 ppm of pollutant, 21 vol% O_2, and N_2 to balance over 50 mg of catalyst.

carried out on the best-performing $CuMnO_x$_redox catalyst.

As reported in Figure S11, for both pollutants and under highly humid conditions, catalytic activity decreased, causing a shift of the conversion curve toward higher temperatures due to the competitive adsorption of water molecules on the surface sites of the catalyst. In the case of CO, the drop in activity at room temperature could probably be related to capillary condensation occurring within the pores of the catalyst, where liquid water can form and partially block access to active sites, slowing down the reaction. However, by increasing the temperature, the catalyst was able to overcome these limitations, possibly because the higher temperature helped to evaporate the condensed water and "open up" the pores again, allowing for complete oxidation of CO at around 125 °C and keeping this full conversion for at least 4 h, as shown by the experimental data. In the case of ethylene oxidation, a less pronounced decrease in conversion was observed under wet conditions. This could be because the oxidation of ethylene typically occurs at higher temperatures, where the impact of moisture and capillary condensation is naturally reduced. Overall, these results were consistent with findings reported in [17,22,83]. Despite the extreme critical conditions, this material performed in a similar way or better than other catalysts [84,85].

Moreover, to better investigate the performance of the $CuMnO_x$_redox sample, a further prolonged TOS analysis was performed by feeding ethylene and alternating dry and wet cycles. The results were reported in Fig. 9.

The catalyst was initially tested under dry feed conditions at 120 °C (Phase I). The C_2H_4 conversion gradually decreased during the first hours but then reached a stable plateau, maintaining an overall conversion of approximately 29 % after 60 h. Subsequently, a fully

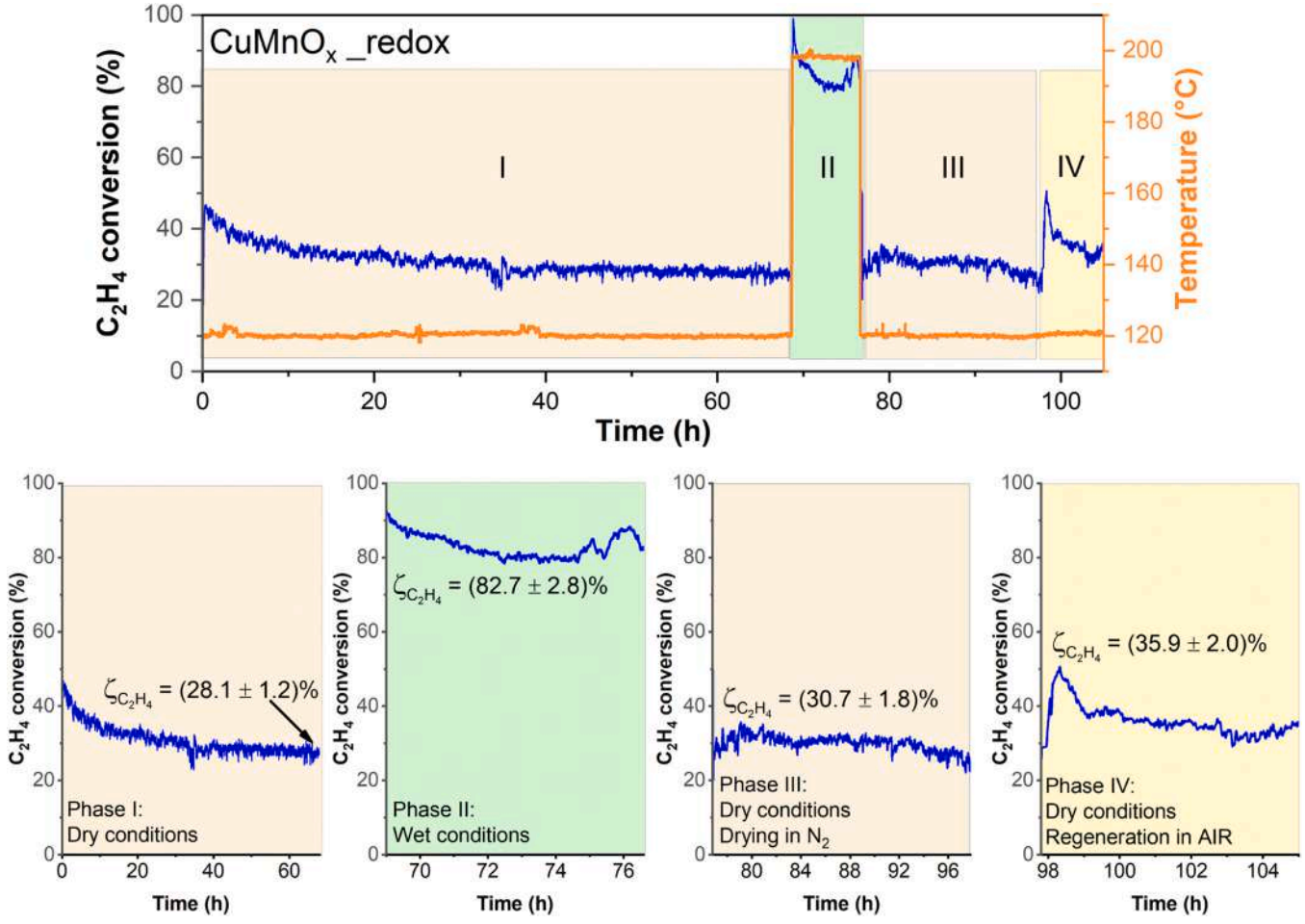

Fig. 9. Time on stream test performed on 50 mg of $CuMnO_x$_redox sample by alternating dry and wet cycles.

saturated wet mixture was fed and a further TOS was repeated, maintaining T_{90} (Phase II). A slight decrease in activity was observed during the first ~2 h, followed by stable performance for the remaining ~6 h of the wet cycle.

Next, the sample was dried in N_2 at 150 °C for 1 h, and another TOS was performed under dry conditions at 120 °C (Phase III). Notably, the catalyst recovered a slightly higher conversion level compared to that observed before the humid TOS (30.7 % compared to 28.1 %), indicating that the N_2 drying step was effective and that the catalyst did not further deactivate in wet conditions. Finally, regeneration was performed in air at 150 °C for 1 h, followed by a further dry TOS (Phase IV). In this case, the conversion increased even more compared to the initial value (ca. 35.9 %), confirming that the short oxidative regeneration was beneficial. Overall, the results demonstrated good long-term stability, even under challenging humid conditions and after extended exposure to the operative conditions.

In conclusion, even under these harsh conditions, the $CuMnO_x$ redox catalyst still performed effectively and stably, highlighting its suitability for real-world applications, where humidity rarely reaches 100 %.

In order to better contextualize the performance of the catalysts developed in this work, a thorough comparison with the existing literature was conducted. Table S3 provides an overview of the most relevant results found in the literature, focusing on systems as similar as possible to those studied in this work. For instance, Wu et al. [86] synthesized a Mn_2CuAlO_x catalyst to simultaneously oxidize CO and reduce NO_x, emphasizing the role of Mn^{3+}/Mn^{4+} redox cycling and abundant surface oxygen species. However, long-term stability tests under realistic conditions were lacking. Similarly, Zhang et al. [87] designed Fe-Mn-Cu mixed oxides for ethylene oxidation, achieving full conversion at 287 °C, with enhanced activity attributed to oxygen vacancies and Fe-Mn-Cu synergies. However, the temperature was quite high, and the work did not explore long-term stability or the effect of pollutant mixtures. Yang et al. [88] performed an *operando* TEM investigation of Cu catalysts for ethylene oxidation, confirming dynamic structural changes occurring during the reaction, but again focusing on more fundamental aspects at the expense of performance evaluation. Liu et al. [89] studied Pt/Al_2O_3 catalyst for enhanced CO oxidation, reaching full conversion at 50 °C, while Zhu et al. [90] studied the evolution of Pt oxidation states during CO oxidation over Pt/CeO_2, highlighting the active role of Pt^{2+}/Pt^0 species and redox cycling with participation of Ce^{4+}/Ce^{3+} pairs. Although both studies reported excellent activity, they relied on expensive noble metals and did not address multicomponent gas mixtures or cost-effective scalability. In contrast, this work demonstrated the low-temperature oxidation of both CO and ethylene without the use of noble metals, achieving full CO conversion at room temperature and 10 % conversion of ethylene at just 85 °C, with long-term stability over 250 h under continuous flow in the case of CO. From this comparison, it became evident that the catalytic system proposed in this work, and especially $CuMnO_x$ redox catalyst, were remarkably competitive. In many cases, they not only outperformed other non-noble metal systems but also surpassed or matched the activity of catalysts based on noble metals. Figure S12 reported a comparison with similar systems in the literature. Although some works showed higher reaction rates, these values are typically obtained at substantially higher temperatures. In contrast, all rates reported in this work were measured at low temperature, within a well-defined kinetic regime, ensuring a rigorous and meaningful comparison. Despite the more stringent conditions, the $CuMnO_x$ redox catalyst developed in this work exhibited competitive or superior performance, highlighting its effectiveness for low-temperature oxidation reactions. What made these results even more significant was the combination of high activity with long-term operational stability. One of the most important advantages of the $CuMnO_x$ redox catalyst was its ability to maintain excellent performance over extended reaction time. Indeed, many catalysts tend to show a quick decline in activity due to deactivation or structural degradation, whereas the $CuMnO_x$ redox sample remained stable and effective throughout the testing period. This robustness, combined with the facile and scalable synthesis and the complete lack of noble metals in the catalyst composition, could represent a high application potential for full-scale industrial implementation.

3.3. Oxidation test with the copresence of pollutants

The simultaneous presence of different pollutants in catalytic reactions introduces additional challenges. And so, multiple contaminants can affect the activity and selectivity of the catalyst. The potential interaction and competition between different pollutants were investigated by using a feed mixture containing 100 ppm of CO and 100 ppm of ethylene in the air over the $CuMnO_x$ redox sample. The results are shown in Fig. 10. Initially, when the temperature was close to room temperature, the catalyst was able to oxidize all incoming CO, showing complete conversion of this pollutant. However, when maintaining the temperature at ca. 20 °C for a sufficiently long time, it was observed that ethylene had a competitive effect on CO. Specifically, when comparing the TOS obtained with a mixture containing only CO to one with CO and C_2H_4, it was found that in the latter case, CO conversion remained at constant at 100 % for over one hour, then slightly decreased and was stabilized at 95 % after 2.5 h. This suggested that, in the presence of multiple pollutants, CO oxidation was affected by the other molecules. On the contrary, ethylene lacks the energy required to break its double bond and to convert it to CO_2 at room temperature. This means that ethylene may adsorb onto the catalyst surface and active sites over time. However, due to insufficient energy provided at reaction temperature, this reactant did not undergo oxidation to CO_2 and remained anchored to the active sites, preventing them from being freed and thus available to CO molecules. As time progressed, the number of sites available for CO activation decreased as they were occupied by ethylene molecules, which did not convert, approaching a steady state after about 2.5 h. Upon increasing the temperature to 50 °C, ethylene began to convert, and the sites previously occupied by this reactant became available again for CO molecules. This suggested that both pollutants may compete for the same activation sites. However, since their activation temperatures are different, the consecutive reaction can occur, converting sequentially ethylene and CO molecules. As the temperature increased further, the reaction rate accelerated, CO remained at 100 % conversion, and ethylene followed the same conversion curve as observed in the absence of CO in the reagent mixture. In fact, comparing the ethylene conversion curves recorded with and without CO present in the reaction mixture, it was found that CO does not affect ethylene conversion. This is a particularly interesting result, highlighting that the only interaction occurred at 25 °C, where CO activation was influenced by the presence of ethylene, but not the other way around.

3.4. Oxidation tests with variable GHSV

In the case of CO oxidation, since the catalyst was extremely active at room temperature, different tests were performed by increasing the value of GHSV to better investigate the performance. For the same reason, in the case of ethylene, GHSV was decreased. The results are reported in Fig. 11 and agree with the literature [91,92]. As a whole, an increase in GHSV provoked a decrease in CO conversion. Specifically, when GHSV was set as $0.3 \times 10^5\ h^{-1}$, CO conversion was 100 % at room temperature. Increasing GHSV, complete oxidation was reached at a slightly higher temperature (less than 75 °C for $0.6 \times 10^5\ h^{-1}$, less than 125 °C for $1.2 \times 10^5\ h^{-1}$, higher than 150 °C for $4.8 \times 10^5\ h^{-1}$). On the contrary, a decrease in GHSV led to an increase in ethylene conversion. When GHSV was $3 \times 10^4\ h^{-1}$, ethylene was fully converted at a temperature lower than 175 °C. Further decreasing GHSV, complete oxidation was reached at 150 °C for both $1.5 \times 10^4\ h^{-1}$ and $0.75 \times 10^4\ h^{-1}$.

In general, this inverse relationship was due to the fact that higher GHSV values correspond to shorter residence times of the pollutant

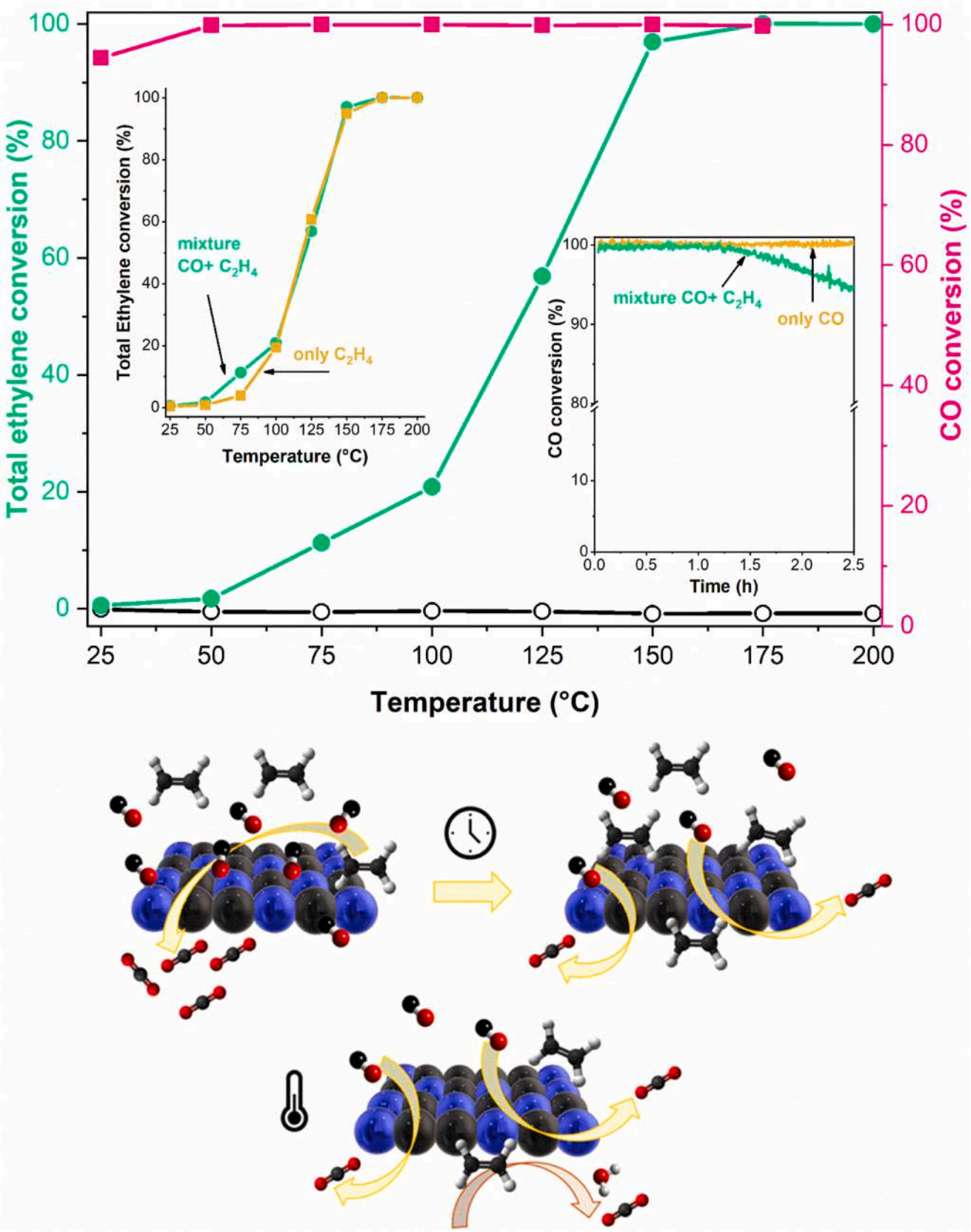

Fig. 10. Catalytic conversion of CO and ethylene as a function of the temperature in dry conditions (up) performed by feeding a gaseous mixture with 100 ppm of CO, 100 ppm C_2H_4, 21 vol% O_2, and N_2 to balance over 50 mg of $CuMnO_x$ redox catalyst (up). A scheme of the proposed mechanism is also reported (down).

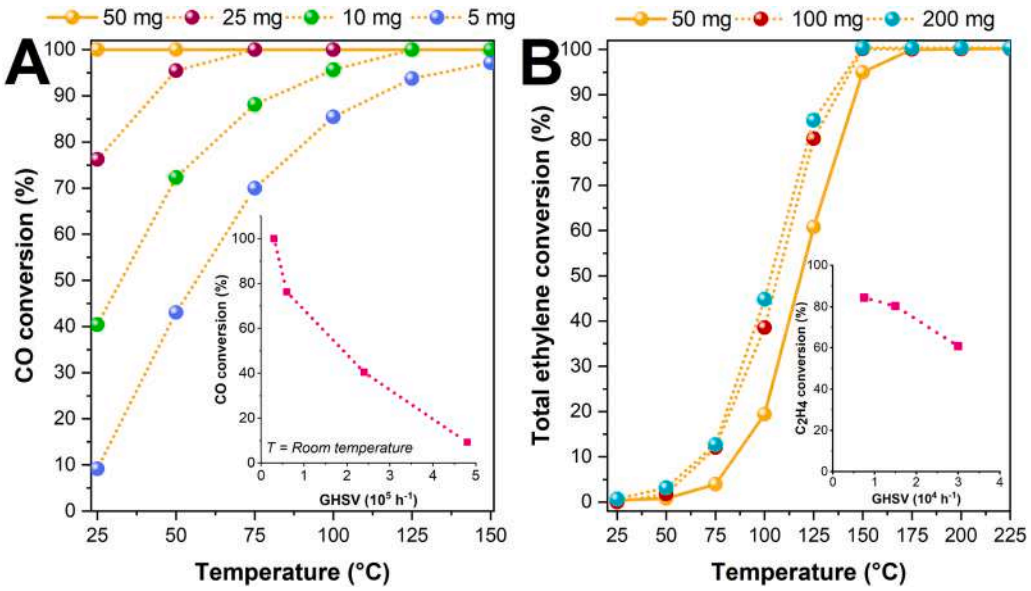

Fig. 11. Catalytic conversion of CO (A) and ethylene (B) as a function of the temperature in dry conditions, performed by feeding a gaseous mixture with 100 ppm of pollutant, 21 vol% O_2, and N_2 to balance and varying GHSV by changing the mass of $CuMnO_x$_redox catalyst in the bed.

within the reactor. Specifically, when GHSV increased, the contact time between the gas-phase reactants (i.e., CO) and the active site of the catalyst was insufficient for the reaction to proceed to a higher extent. In fact, having less time for the interaction between reactants and catalyst, the conversion decreased. GHSV also depended on the catalytic bed volume, and consequently on the mass of catalyst in the reactor. Increasing the GHSV means, in practice, reducing the accessible amount of a sample, and, as a result, the total number of active sites available for the reaction to occur. From this perspective, the outcome was a decrease in conversion. In the case of ethylene, decreasing the GHSV resulted in a longer contact time (at given reaction temperature) between the pollutant (ethylene) and the catalyst, leading to an increase in conversion. However, when the GHSV overcame a threshold, no significant decrease in temperature was observed. This fact highlighted that the unfavorable influence of space velocity on catalytic performance was weak in the range of low GHSV, while the influence became critical when the GHSV was higher than the threshold.

3.5. Correlation between catalytic activity and physico-chemical properties

As revealed by the reported results, the presence of copper significantly enhanced the catalytic performance, and the catalytic activity was highly dependent on the adopted preparation method. Fig. 12 reports the correlation between physico-chemical properties and catalytic activity. Compared to undoped manganese oxide catalysts, the increased activity observed in copper-containing samples could be attributed to a higher number of available active sites due to the higher specific surface area and improved lattice oxygen mobility, as evidenced by both N_2-physisorption and H_2-TPR/O_2-TPD analyses, as well as the formation of smaller crystallites observed via XRD, which makes the sample more reactive [93]. In particular, N_2-physisorption at −196 °C revealed a highly porous structure with elevated SSA, likely contributing to the enhanced catalytic activity compared to the corresponding parent manganese oxides. Moreover, when comparing different copper-containing samples, SSA proved to be a key factor when the difference was substantial, such as between $CuMnO_x$_redox and $CuMnO_x$_oxalate samples compared to the $CuMnO_x$_SCS sample. However, when the surface area difference was smaller (e.g., between $CuMnO_x$_redox and $CuMnO_x$_oxalate), catalytic performance did not necessarily correlate directly with SSA. In fact, although the CuMnOx_oxalate sample exhibited a higher SSA, it showed poorer catalytic performance than the $CuMnO_x$_redox sample, indicating that above a certain threshold, SSA becomes less impactful and other physicochemical properties become important.

Another crucial factor influencing catalytic activity was the presence of reactive oxygen species. Specifically, copper incorporation into the oxide structure weakens Mn-O bonds, promoting the formation and mobility of reactive oxygen species [25]. Even if copper oxide itself shows low intrinsic activity in CO oxidation, as reported by many authors [25,94], combined with manganese oxide in an appropriate ratio, leads to a highly active catalytic system.

Moreover, a crucial aspect of the $CuMnO_x$ catalysts was the presence and role of oxygen vacancies generated upon introduction of Cu^{2+} into the MnO_x matrix. Recent studies, particularly in manganese oxide octahedral molecular sieves (OMS-2), have demonstrated that Cu^{2+} doping significantly increases the concentration of oxygen vacancy defects [79,81,95,96]. Their presence weakens the Mn–O bond strength, increases the amount of surface adsorbed active oxygen species, and improves the mobility of lattice oxygen species, resulting in the significant promotion of the catalytic activity [79] and in an enhancement of catalytic conversion rates [97,98]. This synergy between Cu and Mn played a pivotal role in enhancing oxygen mobility and improving redox properties, as confirmed by XPS, Raman, H_2-TPR, and O_2-TPD analyses.

Temperature-programmed profiles showed that the lower the temperature at which a material is reduced, the more active it tends to be in redox processes. This is related to the greater tendency of the material to release oxygen under reducing conditions, which may reflect the mobility of oxygen species within the bulk. However, it is important to note that TPR is a bulk technique and the relationship between oxygen mobility and surface reaction dynamics is complex. Enhanced oxygen mobility can facilitate surface redox processes, but other factors may also influence catalytic activity [17,70,99]. However, this was especially true in all copper-containing samples. Based on H_2 consumption, $CuMnO_x$_SCS catalyst appeared to have the highest reducibility. However, catalytic results revealed a different trend, explained by considering H_2 uptake across specific temperature ranges. In the low-temperature region (50–200 °C), $CuMnO_x$_redox catalyst exhibited the highest H_2 uptake and, for this reason, it was the most active at low temperatures. In contrast, $CuMnO_x$_SCS catalyst showed higher H_2 consumption in the mid-temperature range, suggesting its greater suitability for applications operating at elevated temperatures. All copper-containing samples also

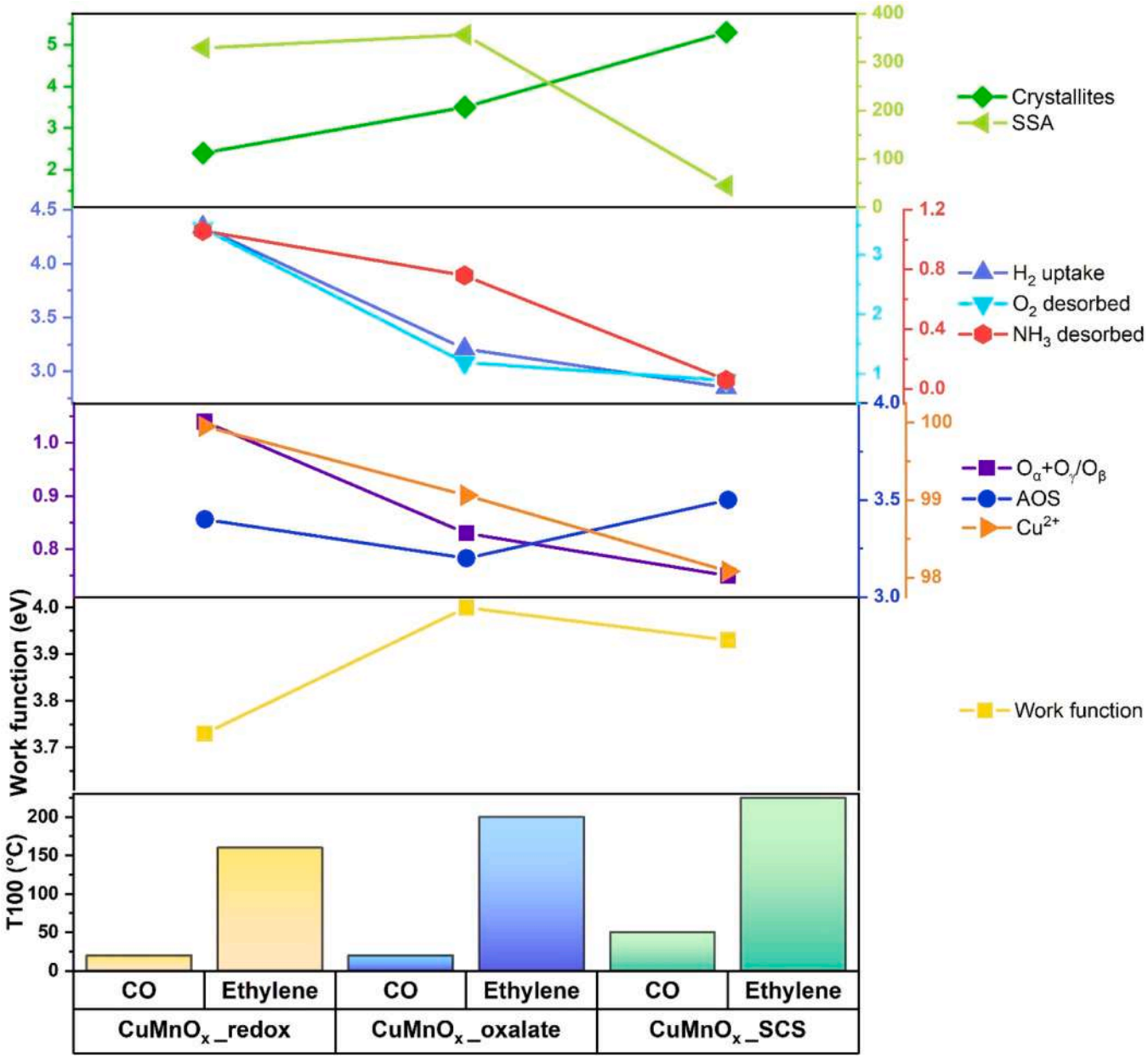

Fig. 12. Correlation between catalytic performances and functional properties of copper-containing samples. Plotted values obtained by H_2-TPR, O_2-TPD, and NH_3-TPD are considered in the range at low temperature of 50–200 °C, 50–250 °C, and 100–250 °C, respectively.

displayed significantly increased concentrations of reactive oxygen species compared to pure manganese oxides, as evidenced by XPS. Particularly, the $CuMnO_x$_redox sample exhibited a high amount of surface oxygen species, including hydroxyls (OH^-), which are known to enhance surface reactivity in many catalytic reactions. For example, Davó-Quiñonero et al. [100] reported that hydroxyls promote the formation of bicarbonates over carbonates, and the catalysts that present high bicarbonate content typically show faster CO oxidation rates. This assumption was confirmed by analyzing the amount of carbonates evaluated from the deconvolution of C1s spectra of the copper-containing samples (not reported here for the sake of brevity). The outcomes revealed that the relative quantity of carbon in the form of carbonates was 8.19 at% in the $CuMnO_x$_redox sample, 10.05 at% in the $CuMnO_x$_SCS sample, and 12.13 at% in the $CuMnO_x$_oxalate sample. This was in line with the trend in activity, showing that catalysts forming more carbonates are less active towards CO oxidation. Moreover, both XPS and catalytic performance suggested that the amount of Mn^{4+} (thus AOS) also plays a key role in determining catalytic efficiency. Literature reports that catalysts with low Mn^{4+} content often show moderated performance [101]. For CO oxidation, the presence and content of tetravalent manganese is crucial, and copper addition can help to enhance both activity and stability [26]. Regarding the oxidation state of copper, XPS analysis showed that almost all copper present is in the Cu^{2+} form (more than 99 % in all samples). Prior studies have demonstrated that the coexistence of Cu^{2+} and Mn^{3+} species is essential for the high catalytic performance of $CuMnO_x$ systems [93].

Another important point concerns the synthesis procedure. The redox method was able to produce compositionally homogeneous $CuMnO_x$ systems, with copper species highly dispersed within an amorphous manganese oxide matrix. Contrary to this, copper–manganese oxides prepared via redox reactions were largely amorphous, and the structural defects related to their poor crystallinity led to the formation of oxygen vacancies, which serve as adsorption centers for oxygen and are highly active in oxidation reactions [26,101,102].

Structural analysis by XRD, TEM, and Raman revealed that the copper-containing catalysts contained two main crystalline phases: $CuMn_2O_4$ and $CuMnO_2$. The former was predominant in the $CuMnO_x$_redox sample (64 %), partially present in the $CuMnO_x$_oxalate (16 %), and absent in the $CuMnO_x$_SCS sample. Thus, both redox and oxalate synthesis methods led to the formation of $CuMn_2O_4$, which was particularly relevant due to the high catalytic activity of this phase in the oxidation of gaseous pollutants, including those examined in this study [93,103].

Finally, catalytic performance can also be correlated with NH_3-TPD results, highlighting the influence of surface acidity on reactivity. The $CuMnO_x$_redox sample, which exhibited the highest total acidity (3.25 mmol g^{-1}) with a well-balanced distribution of weak, medium, and strong acid sites, showed the lowest T_{100} temperatures for both pollutants, confirming the superior activity of this catalyst. In contrast, the $CuMnO_x$_SCS sample, despite having a high concentration of strong acid sites (1.74 mmol g^{-1}), demonstrated only poor activity, suggesting that excessive acid strength may hinder desorption of intermediates or limit their mobility, consistent with its higher T_{100} values. $CuMnO_x$_oxalate sample, with the lowest total acidity (1.46 mmol g^{-1}), showed an intermediate catalytic activity. In summary, catalytic performance in the oxidation of CO and ethylene was strongly influenced by both the quantity and strength of acidic sites. A balanced acidity distribution, as seen in the redox-derived sample, appeared to provide the optimal conditions for promoting low-temperature oxidation reactions.

In the context of heterogeneous catalysis, the work function is defined as the minimum energy required to remove an electron from the surface of a material in vacuum. This property plays a significant role in determining the catalytic activity of metal surfaces. It is closely related to the position of the Fermi level and therefore influences the availability of electrons for interactions with reactant molecules. The work function affects how molecules chemisorb onto the catalyst surface, which is a critical step in many catalytic processes. Additionally, it can change the adsorption of different species (such as oxygen) due to structural modifications of the surface, such as oxidation or doping. These variations, in turn, impact the reactivity and efficiency of the catalyst. A lower work function value is generally advantageous, as it corresponds to a reduced energy barrier for electron transfer to the reactants. This implies a greater availability of surface electrons, which facilitates charge transfer to electron-accepting molecules such as O_2. As a result, reactions, like the oxidation of CO or ethylene, can proceed more readily [104–106]. To the best of the authors' knowledge, no recent studies have established a relationship between the work function and catalytic activity of $CuMnO_x$ systems. However, comparing Cu-containing samples prepared through different synthesis methods, a clear correlation emerges between the low-temperature catalytic performance and the work function results (see Fig. 12). Precisely, the $CuMnO_x$_redox sample, which exhibited the highest catalytic activity, also showed the lowest work function (3.73 eV). In contrast, $CuMnO_x$_SCS and $CuMnO_x$_oxalate exhibited lower catalytic performances due to slightly higher work function values (3.93 eV and 4.00 eV, respectively). Furthermore, when comparing pure MnO_x oxides with their corresponding copper-containing counterparts, the presence of copper was found to affect the work function in different ways. In detail, it decreased from MnO_x_redox (4.03 eV) to $CuMnO_x$_redox (3.73 eV) catalysts, it increased from MnO_x_oxalate (3.81 eV) to $CuMnO_x$_oxalate (4.00 eV) catalysts, and it remained almost unchanged from MnO_x_SCS (3.92 eV) to $CuMnO_x$_SCS (3.93 eV) catalysts. These variations could be related to how copper was incorporated into the oxide structure. In the redox-prepared sample, where the structure was highly homogeneous (as confirmed by EDX mapping, see Fig. 4), copper appeared to be homogeneously distributed in the structure. This structural uniformity may have enhanced the interaction between Cu and Mn species, resulting in a lower work function and improved catalytic performance. Conversely, in the oxalate-derived sample, the less uniform elemental distribution may decrease such synergistic interactions, leading to a slightly higher work function but lower activity compared to the redox sample.

In order to understand which physico-chemical properties mainly control the catalytic activity toward CO and ethylene oxidation over the studied systems, the temperature at which complete oxidation of the pollutant occurs (T_{100}) was correlated with several structural properties of the catalysts, including SSA, crystallite size, O_α/O_β ratio, acidity (ammonia desorbed), AOS, H_2 uptake, and the determined amount of desorbed O_2. For each parameter, the Pearson correlation coefficient (r) was calculated between the parameter value and the T_{100} measured for the copper-containing samples. Although the limited number of samples limits the statistical significance of the analysis, the results could provide useful preliminary insights for identifying the most influential properties affecting catalytic activity. In this context, negative r values indicate a favorable inverse correlation (i.e., as the parameter increases, T_{100} decreases, so the catalyst is more active), while positive values indicate a direct correlation (i.e., as the parameter increases, T_{100} increases and the performance worsens). This correlation analysis was carried out separately for CO and ethylene oxidation to highlight any differences in how each pollutant interacts with the catalysts. Figure S13 reports the outcomes achieved.

For CO oxidation, the parameter that exhibited the strongest inverse correlation is the SSA ($r = -0.99$), indicating that an increased surface area leads to a marked decrease in T_{100} and, consequently, higher activity. The Cu^{2+} and the amount of desorbed ammonia also showed significantly negative correlations ($r = -0.87$ and $r = -0.78$, respectively), suggesting that acidity and copper dispersion played important roles in the reaction. On the other hand, the parameter showing a positive correlation was the AOS ($r = 0.82$), which may indicate that a higher concentration of Mn^{4+} (a more oxidizing form) was associated with higher conversion temperatures, suggesting that excessive AOS may not be optimal for CO activity. Crystallite size ($r = 0.93$) also showed a positive correlation, which aligned with the idea that smaller crystallites favor reactivity.

Regarding ethylene oxidation, the results exhibited clearer and more consistent trends. As a whole, all parameters were strongly correlated with T_{100}, indicating greater sensitivity of the process to structural changes. In particular, the most significant factors were crystallite size, Cu^{2+} species, and the determined amount of desorbed ammonia (all with *r* values close to ±1), indicating that the presence of copper in the oxidized state and the acidic sites were crucial for ethylene activity more than in the case of CO. Other crucial parameters were O_α/O_β ($r = -0.98$), suggesting that reactive oxygen species strongly favored ethylene oxidation, and finally H_2 uptake and desorbed O_2 ($r = -0.96$ and $r = -0.92$, respectively), indicating a correlation between oxygen mobility and catalytic activity.

In summary, in the case of CO oxidation, catalytic activity was primarily driven by structural factors (SSA, sizes of crystallites) and partially also by acidity; whereas, in the case of ethylene, a more multifactorial behavior was expected, where the copper redox state, oxygen mobility, and surface acidic sites were decisive. These results suggested that the nature of the VOC significantly affected the requirements for an optimal catalyst.

However, the T_{100} parameter considers the global process. From a catalytic perspective, the crucial indicator is the reaction rate determined in the kinetic regime, which directly measures catalytic activity. Therefore, Pearson correlation coefficients were also calculated between the reaction rates for ethylene and CO conversion and the physico-chemical properties of the catalysts. The results showed that the rates were strongly influenced by reactive oxygen and the chemical state of copper. Specifically, very high and positive correlations were observed between the rates and parameters such as reactive oxygen concentration O_α/O_β ($r = 0.99$ for C_2H_4 and $r = 0.92$ for rate CO), H_2 uptake ($r \approx 1$ for both), and desorbed O_2 (close to 1). These findings indicated that oxygen species may play a crucial role in catalytic activity. The presence of Cu^{2+} also showed significant positive correlations with the rates (0.93 for C_2H_4, 0.78 for CO), emphasizing the importance of copper as the active

center. Conversely, parameters such as the AOS and SSA showed moderate negative and positive correlations, respectively, while crystallite size exhibited stronger negative correlations (-0.87 for C_2H_4, -0.69 for CO). These data suggested that, in the initial kinetic regime, reaction kinetics were dominated by active sites related to copper and reactive oxygen species, while structural or dispersion-related factors had a less direct influence on the rate.

A comparison of correlation coefficients for T_{100} and rates highlighted distinct roles of the parameters in determining catalytic activity. The rates exhibited strong positive correlations with reactive oxygen species and Cu^{2+} for C_2H_4, whereas parameters like the AOS showed negative or negligible correlations. In contrast, T_{100} often represented stronger inverse correlations with the former parameters and positive correlations with structural parameters such as the AOS and crystallite size. These results indicated that while the rates predominantly reflected intrinsic reaction kinetics, T_{100} was also influenced by structural properties that impacted the temperature required for complete conversion. In summary, evaluating rates alongside T_{100} provided a more comprehensive understanding of catalytic performance, accounting for both kinetic activity and real-world operational conditions.

To further support the structure-activity relationships, a quantitative correlation analysis was performed between the catalytic rates and some key factors (mainly oxygen species O_α/O_β and reducibility, in terms of H_2 uptake at low temperature). As shown in Figure S13, a strong linear relationship was observed for C_2H_4 conversion rates and both the O_α/O_β ratio and the H_2 uptake values. Although the $CuMnO_x$_SCS sample slightly deviated from the linear trend in the case of CO oxidation, probably due to its lower surface area and different redox features, the overall correlation remained high, confirming the critical role of redox and structural properties in catalytic performance. These results clearly demonstrated that the enhanced performance of $CuMnO_x$_redox is strongly associated with its higher content of reactive oxygen and superior reducibility. Notably, these strong correlations also validate the previous trends suggested by the Pearson correlation, where both parameters showed the highest positive correlation with catalytic rates. This quantitative analysis supported the conclusion that oxygen availability and mobility are crucial for low-temperature VOCs oxidation in noble-metal-free catalysts.

This systematic correlation between catalytic activity and physicochemical parameters, including redox properties, oxygen mobility, surface acidity, and work function, fills a clear gap in the literature, as few recent studies have established such a comprehensive structure-activity relationship across different pollutants, addressing both fundamental understanding and catalytic performance, but without trying to figure out the cause-effect relationship between them.

3.6. Reaction mechanisms

Several papers have reported the Mars-van Krevelen (MvK) mechanism to explain the catalytic oxidation of CO and ethylene by $CuMnO_x$ [107,108]. Recent studies highlighted the role of lattice defects and oxygen vacancy concentration, underscoring the key role of active oxygen and defect-rich $CuMnO_x$ interfaces [109].

However, further investigations are necessary to better understand the mechanism at low temperatures and which species are involved. For this reason, the "spent" samples after reaction with CO and ethylene were investigated by XPS. The results for $CuMnO_x$_redox were reported in Fig. 13 and highlighted interesting changes in the distribution of O_α and O_β in the spent catalysts (A, B) compared to the fresh one (C). In particular, an increase in the adsorbed oxygens O_α (+20.0 % for $CuMnO_x$_redox-CO and +30.2 % for $CuMnO_x$_redox-C_2H_4 samples) was observed, compared to lattice oxygen O_β. Besides, the fraction of Mn^{3+} increased with respect to Mn^{4+}, resulting in a decrease in the average oxidation state (AOS) (from 3.4 to 2.3 in both cases) as reported in Table S4.

Moreover, from a deeper analysis of the CuLMM spectral window, a very interesting redistribution of copper species was revealed (see Table S5). First of all, it was noteworthy to mention that, at the end of the reaction, the contents of both Cu^+ and Cu^0 species increased, whereas the contents of Cu^{2+} decreased from 100 % in the fresh catalyst to 92.6 % for the $CuMnO_x$_redox-CO system and 90.8 % for the $CuMnO_x$_redox-C_2H_4 system. Further analysis of the Cu^{2+} species showed that, in all analyzed samples, the CuO component drastically decreased in concentration, while $Cu(OH)_2$ significantly increased, rising from 35.6 % in the fresh sample to 82.3 % in the $CuMnO_x$_redox-CO system and 79.9 % in $CuMnO_x$_redox-C_2H_4. A similar trend was also recorded for the spent $CuMnO_x$_oxalate and $CuMnO_x$_SCS samples, not reported here for the sake of brevity.

To further support this hypothesis, H_2-TPR analysis was performed on the spent catalysts recovered after CO and C_2H_4 oxidation under an oxygen-free atmosphere. Before the TPR, the spent samples were subjected to a pretreatment under He at 120 °C to remove any residual surface contaminants or physisorbed species. The TPR profiles of the spent samples were reported in Figure S14 and exhibited a similar

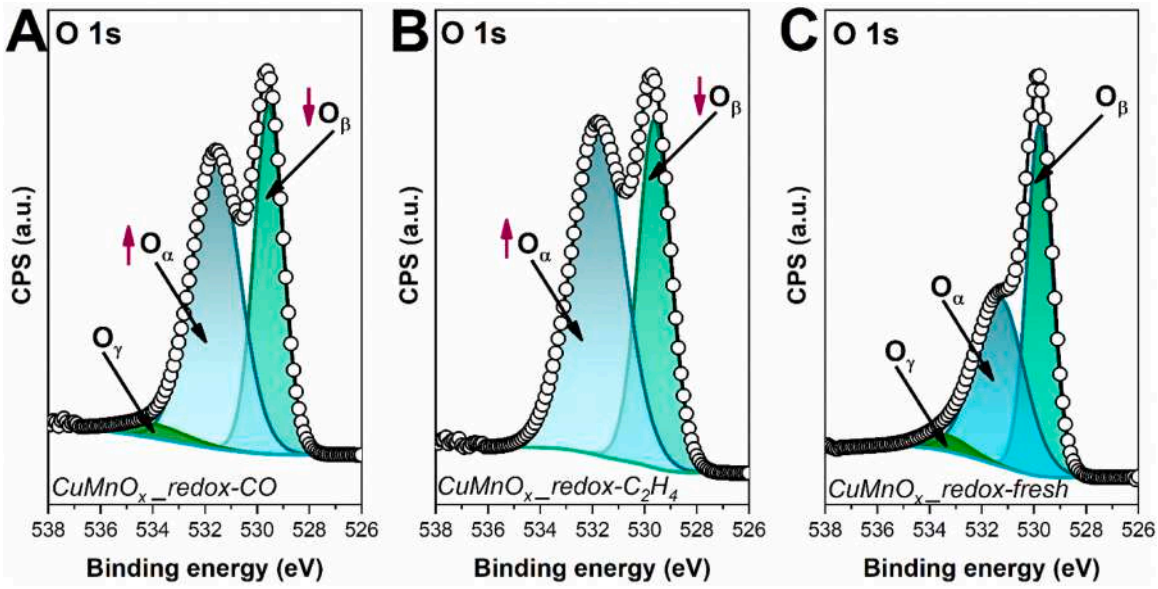

Fig. 13. Variation of oxygen species detected on the spent $CuMnO_x$_redox catalyst after CO (A) and ethylene (B) oxidation and the comparison with the fresh one (C).

reduction pattern to the fresh catalyst but with lower H_2 consumption. This decrease in H_2 uptake strongly suggested that the catalyst was already partially reduced during the reaction, due to the involvement of oxygen species.

Taken together, the catalytic activity in the absence of gas-phase oxygen, the XPS spectra over the spent catalysts, the controlled pre-treatment conditions excluding adsorbed O_2, and the decreased H_2 consumption in TPR all provide converging evidence for a MvK-type mechanism.

3.7. Oxidation test with different pollutant concentrations

Tests by varying the pollutant concentrations were carried out to investigate not only the ability of the $CuMnO_x$ redox catalyst to remove high amounts of pollutants, but also to study possible competitive adsorption between the pollutants and molecular oxygen, giving deeper insight into the reaction mechanism. The results were reported in Figure S15.

For both CO and ethylene, increasing the pollutant concentration resulted in a shift of the conversion curve toward higher temperatures to achieve complete oxidation. For CO, the conversion dropped from 100 % at room temperature under target conditions to approximately 80 % and 60 % when the pollutant concentration was increased by 5 and 10 times, respectively. Despite these much higher concentrations compared to the reference condition, the catalyst still exhibited remarkable performance, maintaining relatively high conversion levels (around 60 %) even at RT. A similar trend was observed for ethylene: increasing its concentration caused a shift in the conversion curve toward slightly higher temperatures, indicating a decrease in performance. In both cases, this behavior could be due to a competitive adsorption effect between molecular oxygen and the pollutant [16]. As the pollutant concentration (either CO or C_2H_4) increased, the catalytically active sites exposed on the catalyst surface became progressively more occupied by the pollutant molecules, reducing the availability of sites to adsorb O_2. This led to a situation analogous to oxygen deficiency at the surface, therefore decreasing catalytic activity. Moreover, for ethylene, a threshold effect was also observed, similar to what was seen in tests with varying GHSV (see Fig. 11). As long as the concentration remained below a certain limit, an increase in C_2H_4 caused a more noticeable shift of the conversion curve (i.e., comparing 100 ppm and 300 ppm). However, once this threshold was surpassed, as in the case from 300 ppm to 500 ppm, the difference became minimal, and in both cases, the maximum conversion was reached at around 200 °C. This behavior suggested that, probably, the molecular oxygen contributed to the oxidation reaction, and that its adsorption was hindered when the active surface was already covered by the pollutant. In fact, when C_2H_4 increased from 100 to 300 ppm, the catalytic surface became closer to the saturation conditions, causing a significant shift in the conversion curve. A further increase in the concentration from 300 to 500 ppm led to only marginal changes because the surface was already largely covered. Therefore, the minimal difference between 300 and 500 ppm could be due to the fact that the active sites were nearly fully occupied by ethylene molecules, so any further increase in concentration had a limited additional effect. The outcomes reached implied a sort of regime of inhibition saturation, where the conversion curve flattened and changed only slightly.

3.8. Oxidation test with different oxygen concentrations

To better investigate the role of oxygen in the reaction mechanism, additional catalytic tests were performed by varying the oxygen concentration (from 21 vol% to 10 vol% and 0 vol%) on the $CuMnO_x$ redox catalyst. The results are displayed in Fig. 14. Overall, by maintaining a constant pollutant concentration (100 ppm) and reducing the oxygen content in the gas mixture from 21 vol% to 10 vol%, a clear decrease in catalytic performance was observed for both CO and ethylene oxidation. This effect was evident in the conversion values: for CO, the conversion dropped from 100 % to 70 % at room temperature, while for ethylene, the conversion decreased from 100 % to 80 % at 175 °C. These results strongly suggested that molecular oxygen played a crucial role in enhancing catalytic activity. Its presence not only increased the availability of reactive oxygen species on the catalyst surface but also helped

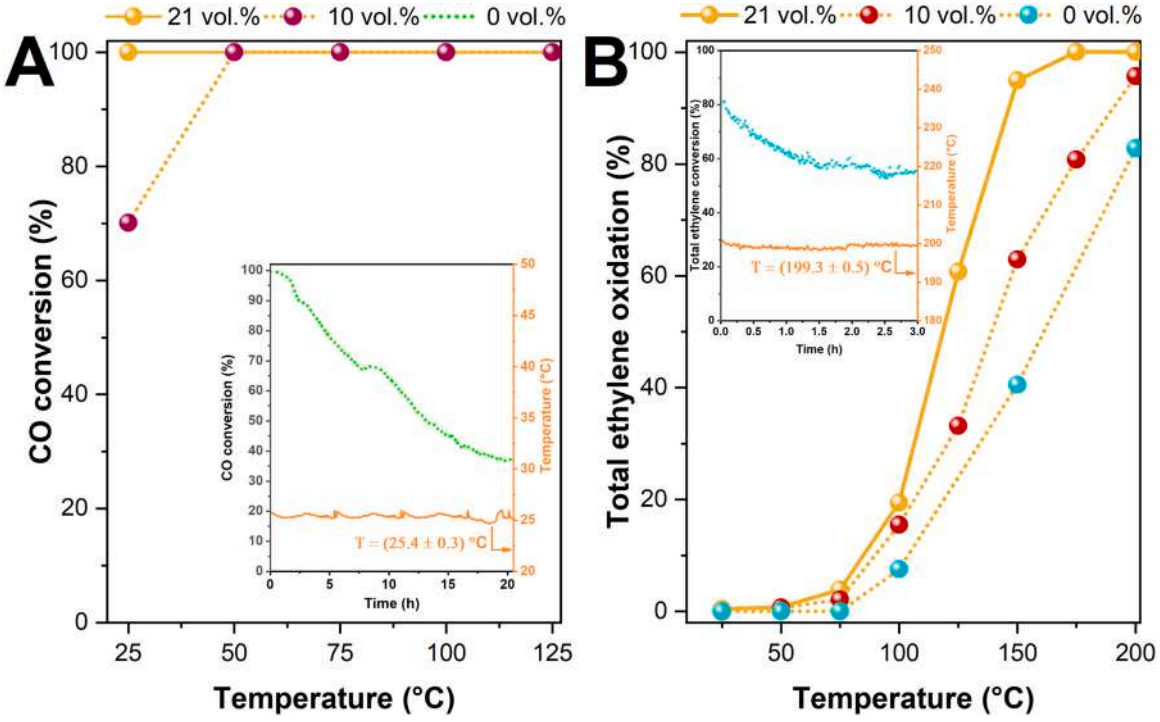

Fig. 14. Catalytic conversion of CO (A) and ethylene (B) as a function of the temperature in dry conditions, performed over $CuMnO_x$ redox by feeding a gaseous mixture with 100 ppm of pollutant and varying the concentration of O_2 from 21 vol% to 0 vol%.

to replenish the lattice oxygen atoms that were consumed during the oxidation process. This behavior aligned with a Mars-van Krevelen type mechanism, where the catalyst actively participates in the redox cycle by providing its own lattice oxygen to oxidize pollutants and subsequently being re-oxidized by molecular O_2.

To further investigate this hypothesis, additional experiments were conducted in the complete absence of oxygen in the gas feed. As shown in Fig. 14, interestingly, even under these oxygen-free conditions, the catalyst was still capable of fully converting CO at room temperature, maintaining this performance for about 2 h. This indicated that the catalyst was able to engage lattice oxygen to carry out the oxidation reaction. However, as the reaction proceeded and these oxygen atoms were gradually depleted, the CO conversion began to decline. Since there was no molecular oxygen in the system to restore the oxidized state of the catalyst, the activity continued to drop, reaching approximately 35 % conversion after 20 h under reactive conditions.

This outcome from this part of results was particularly remarkable, as it highlighted the exceptional ability of the catalyst to operate under such extreme, oxygen-deficient environments. A similar behavior was observed in the case of ethylene oxidation: as the oxygen concentration decreased, the catalytic performance also declined. Moreover, when the catalyst was held isothermally at 200 °C, the conversion gradually decreased, once again due to the progressive consumption of the available oxygen species, which could not be replenished without external molecular oxygen.

These tests effectively provided strong experimental evidence supporting our initial hypothesis about relevance of Mars-van Krevelen-like mechanism, as the catalyst was clearly capable of oxidizing pollutants even in the absence of molecular oxygen. At the same time, they underscored the importance of O_2 in sustaining long-term catalytic activity; without it, the catalyst eventually lost its ability to perform at high levels. Therefore, both the redox flexibility of the catalyst and the presence of molecular oxygen were essential components that governed its overall efficiency and durability in oxidation reactions at low temperatures.

The results obtained from XPS carried out on the spent powders, in addition to the catalytic tests performed under different pollutant concentrations and oxygen concentrations, suggested a catalytic mechanism governed by both Mars-van Krevelen redox cycles and controlled by oxygen mobility, as well as by the influence of molecular oxygen. More specifically, the results demonstrated a possible simultaneous synergy of two different mechanisms in the low temperature range. Indeed, the oxygen species responsible for pollutant oxidation were derived from both surface/lattice oxygen and molecular oxygen. On one hand, molecular oxygen from air, adsorbing on active surface sites, was activated thanks to exposed redox species such as Cu^{+}/Cu^{2+} and Mn^{3+}/Mn^{4+}, generating highly reactive species like O^{-}, O_2^{-}, and O_2^{2-} [110,111]. On the other hand, lattice oxygen can further participate in the reaction. During the reaction, CO and ethylene are oxidized by these reactive oxygen species, with the consequent reduction of Mn^{4+} to Mn^{3+} and Cu^{2+} to Cu^{+}, as evidenced by the deconvolution of the spectra. Mn^{4+} and Cu^{2+} act as oxidizing centers and are reduced to Mn^{3+} and Cu^{+}, respectively. Furthermore, the decrease in the concentration of bulk oxygen O_β implied that the bulk oxygen derived from Mn-O-Cu, which was more labile, migrated to the surface and reacted with the pollutant according to a MvK-type mechanism, highlighting that the metal oxide lattice served as a different oxygen source [16,108]. Moreover, as reported by other authors [81,112], the active site in $CuMnO_x$ catalysts, especially for CO oxidation, has been proposed as a surface Cu^{2+}–O^{2}–Mn^{4+} bridge, with lattice oxygen participating in the MvK mechanism and vacancies (□) at Cu^{2+}–□–Mn^{3+} sites allowing O_2 re-adsorption and catalyst regeneration. Finally, the presence of a higher amount of Mn^{3+} and Cu^{+} observed in the spent samples compared to the fresh ones may suggest incomplete or slow regeneration of the catalyst under the adopted operating conditions. Similar trends were also confirmed in other studies [16,111].

Table 9
Quantitative variation of reactive species at the catalyst surface during CO and ethylene oxidation, as revealed by analyzing the spent catalyst through XPS.

Species	Variation	Explanation
O_α	↑	Due to molecular O_2 adsorption and lattice oxygen migration toward the surface → O^{-}, O_2^{-}, O_2^{2-} species were formed
O_β	↓	Lattice oxygen participated in the reaction to oxidize CO/C_2H_4 → MvK mechanism
Mn^{3+}	↑	Mn^{4+} was reduced to Mn^{3+} during the reaction. Possible accumulation at the end of the reaction if regeneration is incomplete or slow
Cu^{+}	↑	Cu^{2+} was reduced to Cu^{+} during the reaction. Possible accumulation at the end of the reaction if regeneration is incomplete or slow

In conclusion, the results were summarized in Table 9 and it was possible to assume that a functional synergy between Cu and Mn occurred in the catalyst structure, where the two metals facilitate the activation and transfer of oxygen thanks to the presence and formation of Cu-O-Mn bonds that promote electron exchange and oxygen mobility on the surface.

To gain deeper insight into the oxidation mechanism of both pollutants, in-situ DRIFTS analyses were performed, and the results are presented in Fig. 15, Figure S16 and Figure S17.

In the case of CO, during *Phase 1* (A), carried out under an oxygen-free atmosphere, a band located at 2120 cm^{-1} initially appeared, and it was ascribed to CO adsorbed on the catalyst surface [80,113,114]. In addition to this, a peak located at 2347 cm^{-1} appeared, assigned to the presence of physisorbed CO_2, which gradually decreased over time. As CO was continuously fed to the catalyst under oxygen-free conditions, the carbonyl peak increased in intensity, while the CO_2 band progressively decreased over time, due to the depletion of oxygen from the catalyst, and the peak stabilized after 60 min. Interestingly, a shift of the carbonyl band was observed, from 2120 cm^{-1} at t_0 to 2112 cm^{-1} at t = 60 min. This shift could be due to CO adsorption on Cu^{+} sites [80]. According to XPS analysis on the spent sample (see Fig. 13), the fresh one predominantly contained Cu^{2+}, but an increase in Cu^{+} species and a decrease in the AOS were previously observed at the end of the reaction. Therefore, the observed shift may be explained by the progressive reduction of the surface under CO flow, leading to a higher concentration of Cu^{+} sites, which in turn provided more coordination sites for CO. In the 1700–1300 cm^{-1} region (see Figure S16), the bands attributed to the surface carbonates [37,115–117] gradually increased in intensity over time, indicating their accumulation on the catalyst surface. During *Phase 2* (static conditions, with the gas flow switched to by-pass), the pollutant feed was stopped, but the reaction mixture remained inside the cell, simulating a batch reactor (B). Over time, the intensity of the carbonyl band decreased, while that characteristic of CO_2 increased, suggesting that even in the absence of gaseous O_2, the catalyst was able to oxidize CO engaging lattice oxygen, which resulted in CO_2 production. Concerning the carbonate-related bands, these species continued to increase, indicating further deposition on the surface. To remove these residues and to regenerate the catalyst, mimicking a typical redox cycle, air was introduced in *Phase 3* (C). Under these conditions, both CO_2 and CO residues were fully removed, and the intensity of the carbonate bands significantly decreased, indicating partial surface regeneration. Increasing the temperature (*Phase 4*), the carbonyl-related bands completely disappeared, and carbonate bands further decreased, provoking additional CO_2 formation (D). By the end of this phase, the DRIFTS spectra showed that the catalyst surface had largely returned to the same state as that observed after the initial pretreatment, confirming the successful reoxidation and regeneration of the sample.

The results related to ethylene are shown in Fig. 15 (E-H) and Figure S16 (E, F). During *Phase 1* (E), when the ethylene reached the catalyst surface at room temperature, the peak between 2350 and 2300

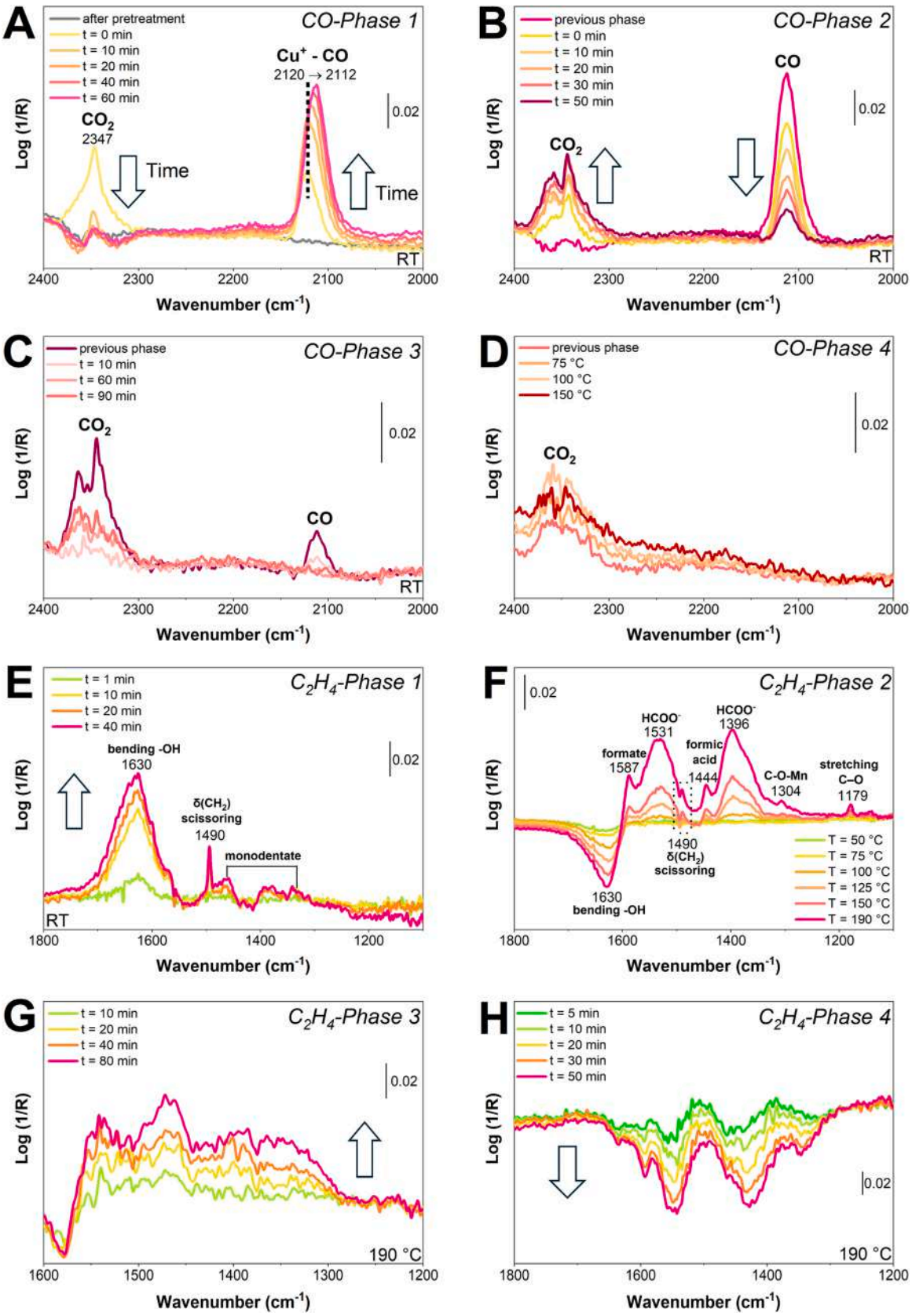

Fig. 15. DRIFTS spectra collected over time and temperature for CO (A-D) and ethylene (E-H) using $CuMnO_x$ redox catalyst. Spectra in Figures (E-H) are reported in difference.

cm^{-1}, attributed to physisorbed CO_2, increased. During the first 20 min of exposure, the intensity of this band increased, suggesting a possible oxidation of ethylene already occurring at room temperature due to the presence of oxygen species of the catalyst. Subsequently, the CO_2 signal gradually decreased, probably due to the consumption of oxygen (see Figure S16). No bands corresponding to carbonyl intermediates (2120 cm^{-1}) were detected, as in the CO experiments. On the other hand, in the 1700–1300 cm^{-1} region, an increase in bands related to carbonate species was observed [118]. These species were already present on the catalyst surface after the pretreatment, but their intensity increased upon ethylene exposure. Notably, a new band appeared at 1490 cm^{-1} after just 10 min, which was assigned to the $\delta(CH_2)$ scissoring mode, characteristic of short hydrocarbon chains such as acetate groups or adsorbed ethylene fragments [119]. Additionally, the band at 1630 cm^{-1}, attributed to the bending mode of adsorbed -OH, also increased slightly. The increase of this last peak could be due to a possible formation of hydrogen, coming from the dissociation of chemisorbed ethylene, which reacts with the oxygen of the catalyst to form -OH groups [120]. Increasing the temperature from room temperature to 200 °C (*Phase 2*), -OH may recombine into H_2O and desorb, leading to the disappearance of the 1630 cm^{-1} band. On the other hand, the CO_2 band did not increase so much, whereas the region between 1600 and 1100 cm^{-1} underwent significant changes (F). In particular, bands at 1490, 1444, 1304, and 1179 cm^{-1} became more pronounced when the temperature was 125 °C. These peaks were attributed to acetates or adsorbed ethylene [119], physical adsorption of formic acid [121], C-O-Mn vibrations [122], and C-O stretches of acetate or formate species [119]. Peaks at 1490 and 1179 cm^{-1} did not appear when the same experiment was repeated in the presence of oxygen (Figure S18 and Figure S19), indicating that these intermediates only formed under oxygen-free conditions, as products of partial oxidation. In *Phase 3*, with the reactor kept in static conditions (gas in by-pass), ethylene remained inside the cell (G). During the initial minutes, a slight increase in CO_2 was recorded, confirming that the catalyst could still oxidize ethylene using its own oxygen. As expected, when this oxygen was consumed, the CO_2 band decreased, while the carbonate bands showed a minor increase. Finally, in *Phase 4* (H), air was introduced at ≈ 200 °C. A progressive decrease in the bands related to carbonates and other intermediates was observed, indicating the removal of surface species. By the end of this phase, the DRIFTS spectrum closely resembled that of the pretreated catalyst, confirming that the surface had been largely regenerated under oxidizing conditions.

4. Conclusions

In this work, several optimized synthetic routes were proposed with the aim of developing highly active and efficient catalysts for the removal of such gaseous pollutants as CO and C_2H_4. These materials were obtained using simple, rapid, and easily scalable methods, without using expensive noble metals to enhance their performance. Thanks to their outstanding activity, these materials also showed great potential for indoor air purification. In particular, the $CuMnO_x$_redox sample was able to completely oxidize CO even at room temperature, maintaining full conversion for several hours. Specifically, this catalyst maintained 100 % conversion for 6 h and over 90 % for the other 244 h, outperforming most reported systems. Moreover, the $CuMnO_x$_redox sample showed measurable CO conversion even with extremely low amounts (5 mg), confirming its high activity and potential for practical applications. Although slightly higher temperatures were required for ethylene, a T_{10} of 85 °C was achieved with this catalyst. The $CuMnO_x$_redox sample also showed excellent performance under more demanding conditions, such as with high pollutant concentrations (five or ten times higher than typical), in the complete absence of oxygen, in the presence of moisture, and even in the presence of multiple pollutants introduced simultaneously. The performances of these materials clearly surpassed those reported in the literature. Their competitiveness was further enhanced by the absence of noble metals, making them viable for potential commercialization. The enhanced activity was attributed to a combination of factors, i.e., the high content of reactive oxygen species and improved oxygen mobility, driven by the synergistic interaction between Cu and Mn in the catalyst structure, which weakened the metal-oxygen interactions and promoted the formation of oxygen vacancies. Moreover, the catalysts exhibited remarkably high surface areas, exceeding values typically reported in the literature. The predominantly amorphous matrix led to structural discontinuities, which contributed to an increased density of defects, boosting catalytic performance. Notably, a systematic correlation between the physico-chemical parameters and catalytic performance (both in terms of T_{100} and reaction rates) was established for the two pollutants investigated. This showed that the key factors differ depending on the molecule (CO or ethylene). In addition, the work function was demonstrated to correlate with activity, offering a new electronic descriptor for the design of future CuMn-based catalysts. These findings highlighted the promise of these materials for low-temperature pollutant abatement and their potential contribution to improving air quality and human well-being in enclosed environments.

CRediT authorship contribution statement

Nadia Grifasi: Conceptualization, Data curation, Formal analysis, Investigation, Methodology, Visualization, Writing – original and reviewed draft. **Enrico Sartoretti:** Formal analysis, Investigation, Writing - original and reviewed draft. **Piotr Legutko:** Data curation, Formal analysis, Investigation, Writing - original draft. **Samir Bensaid:** Supervision, Writing- original and reviewed draft. **Nunzio Russo:** Supervision, Writing- original and reviewed draft. **Andrzej Adamski:** Supervision, Writing - original and reviewed draft. **Debora Fino:** Funding. **Marco Piumetti:** Conceptualization, Supervision, Writing-original and reviewed draft.

Funding

This study was carried out within the Guardian project – funded by European Union – Next Generation EU, within the PRIN 2022 PNRR program (D.D. 1409 del 14/09/2022 Ministero dell'Università e della Ricerca). This manuscript reflects only the authors' views and opinions and the Ministry cannot be considered responsible for them. The Raman analysis was carried out using research infrastructure funded by the European Union in the framework of the Smart Growth Operational Programme, Measure 4.2; Grant No. POIR.04.02.00–00-D001/20, "ATOMIN 2.0- Center for materials research on ATOMic scale for the INnovative economy".

Declaration of Competing Interest

The authors declare that they have no known competing financial interests or personal relationships that could have appeared to influence the work reported in this paper.

Acknowledgment

The authors thank Camilla Galletti for XRD measurement, Antoine Miche for XPS on the fresh catalysts, and Marco Allione for HR-TEM analyses. The authors also acknowledge the PON Ricerca e Innovazione "REACT-EU" project (DM 1062/21) and the funding received by Ministero dell'Università e della Ricerca under the Dipartimento di Eccellenza 2018-2022 program. Finally, the authors also thank Marco Pietro Mezzapesa and Dr. Andrea Rizzetto for their help during DRIFTS measurement and elaboration.

Appendix A. Supporting information

Supplementary data associated with this article can be found in the

online version at doi:10.1016/j.apcatb.2025.126292.

Data availability

Data will be made available on request.

References

[1] V. Carvajal, J.V. Jorques Molla, Y. Luo, Y. Zhao, G. Moncunill, M. Gascon, Air pollution and systemic immune biomarkers in early life: a systematic review, Environ. Res 269 (2025) 120838, https://doi.org/10.1016/j.envres.2025.120838.

[2] Y. Guo, M. Wen, G. Li, T. An, Recent advances in VOC elimination by catalytic oxidation technology onto various nanoparticles catalysts: a critical review, Appl. Catal. B 281 (2021), https://doi.org/10.1016/j.apcatb.2020.119447.

[3] United States Environmental Protection Agency Volatile Organic Compounds' Impact on Indoor Air Quality, US EPA. United States government 2022.2022.

[4] US; Environmental Protection Agency; U.S. EPA. An Introduction to Indoor Air Quality: Volatile Organic Compounds (VOCs). 2011.

[5] G. Settimo, M. Manigrasso, P. Avino, Indoor Air Quality: A Focus on the European Legislation and State-of-the-Art Research in Italy, Atmosphere (Basel) 11 (2020).

[6] A. Lepore, V. Ubaldi, B. Silvia, Inquin. Indoor. Aspetti Gen. e Casi Stud. Ital. (2010). ISBN 978-88-448-0451-0.

[7] J.-Y. Chin, C. Godwin, E. Parker, T. Robins, T. Lewis, P. Harbin, S. Batterman, Levels and Sources of Volatile Organic Compounds in Homes of Children with Asthma, Indoor Air 24 (2014) 403–415, https://doi.org/10.1111/ina.12086.

[8] Z. Bai, Z. Wang, T. Zhu, J. Zhang, Developing Indoor Air Quality Related Standards in China, J. Asian Archit. Build. Eng. 2 (2003) 55–60, https://doi.org/10.3130/jaabe.2.55.

[9] L. Song, J. Zhou, C. Wang, G. Meng, Y. Li, M. Jarin, Z. Wu, X. Xie, Airborne Pathogenic Microorganisms and Air Cleaning Technology Development: A Review, J. Hazard Mater. 424 (2022) 127429, https://doi.org/10.1016/j.jhazmat.2021.127429.

[10] R. Zhao, H. Wang, D. Zhao, R. Liu, S. Liu, J. Fu, Y. Zhang, H. Ding, Review on catalytic oxidation of VOCs at ambient temperature, Int J. Mol. Sci. 23 (2022), https://doi.org/10.3390/ijms232213739.

[11] J. González-Martín, N.J.R. Kraakman, C. Pérez, R. Lebrero, R. Muñoz, A state–of–the-art review on indoor air pollution and strategies for indoor air pollution control, Chemosphere 262 (2021) 128376, https://doi.org/10.1016/j.chemosphere.2020.128376.

[12] D. Gu, J.-C. Tseng, C. Weidenthaler, H.-J. Bongard, B. Spliethoff, W. Schmidt, F. Soulimani, B.M. Weckhuysen, F. Schüth, Gold on different manganese oxides: ultra-low-temperature CO oxidation over colloidal gold supported on bulk-MnO2 nanomaterials, J. Am. Chem. Soc. 138 (2016) 9572–9580, https://doi.org/10.1021/jacs.6b04251.

[13] L.-C. Wang, Q. Liu, X.-S. Huang, Y.-M. Liu, Y. Cao, K.-N. Fan, Gold nanoparticles supported on manganese oxides for low-temperature CO oxidation, Appl. Catal. B 88 (2009) 204–212.

[14] H. Yang, C. Ma, G. Wang, Y. Sun, J. Cheng, Z. Zhang, X. Zhang, Z. Hao, Fluorine-enhanced Pt/ZSM-5 catalysts for low-temperature oxidation of ethylene, Catal. Sci. Technol. 8 (2018) 1988–1996.

[15] H. Chen, R. Zhang, H. Wang, W. Bao, Y. Wei, Encapsulating uniform Pd nanoparticles in TS-1 zeolite as efficient catalyst for catalytic abatement of indoor formaldehyde at room temperature, Appl. Catal. B 278 (2020), https://doi.org/10.1016/j.apcatb.2020.119311.

[16] K. Wang, K. Li, S. Zhao, Z. Ran, F. Wang, Experimental and mechanism investigation on CO Catalytic oxidation performance based on CuMn2O4 catalysts, Appl. Catal. A Gen. 692 (2025) 120091.

[17] N. Grifasi, E. Sartoretti, D. Montesi, S. Bensaid, N. Russo, F.A. Deorsola, D. Fino, C. Novara, F. Giorgis, M. Piumetti, Mesostructured manganese oxides for efficient catalytic oxidation of CO, ethylene, and propylene at mild temperatures: insight into the role of crystalline phases and physico-chemical properties, Appl. Catal. B Environ. Energy 362 (2025) 124696.

[18] F. Kong, H. Zhang, H. Chai, B. Liu, Y. Cao, Insight into the crystal structures and surface property of manganese oxide on CO catalytic oxidation performance, Inorg. Chem. 60 (2021) 5812–5820.

[19] V. Bratan, A. Vasile, P. Chesler, C. Hornoiu, Insights into the redox and structural properties of CoOx and MnOx: fundamental factors affecting the catalytic performance in the oxidation process of VOCs, Catalysts 12 (2022).

[20] S. Dey, G.C. Dhal, D. Mohan, R. Prasad, Low-temperature complete oxidation of CO over various manganese oxide catalysts, Atmos. Pollut. Res 9 (2018) 755–763.

[21] H. Huang, Y. Xu, Q. Feng, D.Y.C. Leung, Low Temperature catalytic oxidation of volatile organic compounds: a review, Catal. Sci. Technol. 5 (2015) 2649–2669.

[22] C. Cocuzza, E. Sartoretti, C. Novara, F. Giorgis, S. Bensaid, N. Russo, D. Fino, M. Piumetti, Copper-manganese oxide catalysts prepared by solution combustion synthesis for total oxidation of VOCs, Catal. Today 423 (2023) 114292, https://doi.org/10.1016/j.cattod.2023.114292.

[23] E.C. Njagi, C.-H. Chen, H. Genuino, H. Galindo, H. Huang, S.L. Suib, Total oxidation of CO at ambient temperature using copper manganese oxide catalysts prepared by a redox method, Appl. Catal. B 99 (2010) 103–110, https://doi.org/10.1016/j.apcatb.2010.06.006.

[24] X. Hu, J. Chen, S. Li, Y. Chen, W. Qu, Z. Ma, X. Tang, The promotional effect of copper in catalytic oxidation by Cu-doped α-MnO2 nanorods, J. Phys. Chem. C. 124 (2020) 701–708, https://doi.org/10.1021/acs.jpcc.9b09891.

[25] S. Dey, G.C. Dhal, D. Mohan, R. Prasad, Synthesis of silver promoted CuMnOx catalyst for ambient temperature oxidation of carbon monoxide, Journal Science Advanced Materials Devices 4 (2019) 47–56.

[26] J.P.N. Kembo, J. Wang, N. Luo, F. Gao, H. Yi, S. Zhao, Y. Zhou, X. Tang, A review of catalytic oxidation of carbon monoxide over different catalysts with an emphasis on hopcalite catalysts, N. J. Chem. 47 (2023) 20222–20247.

[27] M. Dosa, M.J. Marin-figueredo, E. Sartoretti, C. Novara, F. Giorgis, S. Bensaid, D. Fino, N. Russo, M. Piumetti, Cerium-copper oxides synthesized in a multi-inlet vortex reactor as effective nanocatalysts for CO and ethene oxidation reactions, Catalysts 12 (2022), https://doi.org/10.3390/catal12040364.

[28] N. Keller, M.-N. Ducamp, D. Robert, V. Keller, Ethylene removal and fresh product storage: a challenge at the frontiers of chemistry. Toward an approach by photocatalytic oxidation, Chem. Rev. 113 (2013) 5029–5070, https://doi.org/10.1021/cr900398v.

[29] E.A. AKMANThe impact of indoor pollutants on children's health.50. environmental factors and child health.

[30] K. Frey, V. Iablokov, G. Sáfrán, J. Osán, I. Sajó, R. Szukiewicz, S. Chenakin, N. Kruse, Nanostructured MnO x as Highly Active Catalyst for CO Oxidation, J. Catal. 287 (2012) 30–36, https://doi.org/10.1016/j.jcat.2011.11.014.

[31] V. Iablokov, K. Frey, O. Geszti, N. Kruse, High Catalytic Activity in CO Oxidation over MnOx Nanocrystals, Catal. Lett. 134 (2010) 210–216, https://doi.org/10.1007/s10562-009-0244-0.

[32] B.D. Cullity, UoNotreDame Elem. Diffr. QuasiOpt. (1994). ISBN 0201011743.

[33] D. Penney, V. Benignus, S. Kephalopoulos, et al., Carbon Monoxide. In: WHO Guidelines for Indoor Air Quality: Selected Pollutants, World Health Organization, *Geneva*, 2010.

[34] M. Thommes, K. Kaneko, A.V. Neimark, J.P. Olivier, F. Rodriguez-Reinoso, J. Rouquerol, K.S.W. Sing, Physisorption of Gases, with Special Reference to the Evaluation of Surface Area and Pore Size Distribution (IUPAC Technical Report) 87 (2015) 1051–1069, https://doi.org/10.1515/pac-2014-1117.

[35] R.D. t Shannon, C.T. Prewitt, Effective ionic radii in oxides and fluorides, Struct. Sci. 25 (1969) 925–946.

[36] E. Sartoretti, C. Novara, A. Chiodoni, F. Giorgis, M. Piumetti, S. Bensaid, N. Russo, D. Fino, Nanostructured ceria-based catalysts doped with La and Nd: how acid-base sites and redox properties determine the oxidation mechanisms, Catal. Today 390 (2022) 117–134.

[37] A. Rizzetto, E. Sartoretti, M. Piumetti, R. Pirone, S. Bensaid, Novel application of Ru-based catalysts on MgAl oxides alkaline adsorbents for Cyclic CO2 methanation, Chem. Eng. J. 501 (2024) 157585.

[38] C.M. Julien, M. Massot, C. Poinsignon, Lattice vibrations of manganese oxides: Part I. periodic structures, Spectrochim. Acta A Mol. Biomol. Spectrosc. 60 (2004) 689–700.

[39] Q. Yang, Y. Tang, H. Zhang, J. Chen, Z. Jiang, K. Xiong, J. Wang, X. Liu, N. Yang, Q. Du, Classic deep oxidation CuMnOx catalysts catalyzed selective oxidation of benzyl alcohol, Appl. Surf. Sci. 610 (2023) 155364.

[40] C. Xuan, S. Han, L. Wang, X. Zhang, R. Sun, X. Cheng, Z. Wang, C. Ma, T. Zhao, X. Hou, Mechanism of NO Reduction by NH 3 over CuMnO x Catalysts and the Influence Mechanism of CO, Catal. Sci. Technol. 13 (2023) 3106–3124.

[41] Crednerite R070404, RRUFF Databse. (n.d.). ⟨Https://Rruff.Info/Crednerite⟩.

[42] P. Legutko, M. Fedyna, J. Gryboś, X. Yu, Z. Zhao, A. Adamski, A. Kotarba, Z. Sojka, Intricate role of doping with D0 Ions (Zr4+, V5+, Mo6+, W6+) on cryptomelane (K-OMS-2) performance in the catalytic soot combustion in presence of NO and SO2, Fuel 328 (2022) 125325.

[43] P. Stelmachowski, P. Legutko, T. Jakubek, A. Kotarba, Phase evolution and electronic properties of cryptomelane nanorods, J. Alloy. Compd. 767 (2018) 592–599.

[44] B. Saravanakumar, S.M. Lakshmi, G. Ravi, V. Ganesh, A. Sakunthala, R. Yuvakkumar, Electrochemical properties of rice-like copper manganese oxide (CuMn2O4) nanoparticles for pseudocapacitor applications, J. Alloy. Compd. 723 (2017) 115–122.

[45] J. Wang, J. Chen, L. Peng, H. Zhang, Z. Jiang, K. Xiong, Q. Yang, J. Chen, N. Yang, On the CuO-Mn2O3 Oxide-Pair in CuMnOx Multi-Oxide Complexes: Structural and Catalytic Studies, Appl. Surf. Sci. 575 (2022) 151733.

[46] V.P. Santos, M.F.R. Pereira, J.J.M. Órfão, J.L. Figueiredo, The Role of Lattice Oxygen on the Activity of Manganese Oxides towards the Oxidation of Volatile Organic Compounds, Appl. Catal. B 99 (2010) 353–363, https://doi.org/10.1016/j.apcatb.2010.07.007.

[47] X. Duan, T. Zhao, Z. Yang, B. Niu, G. Li, B. Li, Z. Zhang, J. Cheng, Z. Hao, Oxygen Activation-Boosted Manganese Oxide with Unique Interface for Chlorobenzene Oxidation: Unveiling the Roles and Dynamic Variation of Active Oxygen Species in Heterogeneous Catalytic Oxidation Process, Appl. Catal. B 331 (2023) 122719.

[48] H. Radinger, P. Connor, R. Stark, W. Jaegermann, B. Kaiser, Manganese Oxide as an Inorganic Catalyst for the Oxygen Evolution Reaction Studied by X-Ray Photoelectron and Operando Raman Spectroscopy, ChemCatChem 13 (2021) 1175–1185, https://doi.org/10.1002/cctc.202001756.

[49] Stranick, M.A.; Stranick, M.A. MnO2 by XPS MnO 2 by XPS. *Surface Science Spectra* 2015, *6*, 31.

[50] H.W. Nesbitt, D. Banerjee, Interpretation of XPS Mn(2p) Spectra of Mn Oxyhydroxides and Constraints on the Mechanism of MnO2 Precipitation, Am. Mineral. 83 (1998) 305–315, https://doi.org/10.2138/am-1998-3-414.

[51] M.J. Marin Figueredo, M. Piumetti, S. Bensaid, D. Fino, R. Nunzio, Catalytic Oxidation of Volatile Organic Compounds over Porous Manganese Oxides Prepared via Sol-Gel Method, Nanostruct. Catal. Environ. Appl. (2021) 59–78, https://doi.org/10.1007/978-3-030-58934-9_2.

[52] M. Piumetti, D. Fino, N. Russo, Mesoporous manganese oxides prepared by solution combustion synthesis as catalysts for the total oxidation of VOCs, Appl. Catal. B 163 (2015) 277–287, https://doi.org/10.1016/j.apcatb.2014.08.012.
[53] Y. Wei, S. Jin, R. Zhang, W. Li, J. Wang, S. Yang, H. Wang, M. Yang, Y. Liu, W. Qiao, et al., Preparation of Mesoporous Mn-Ce-Ti-O Aerogels by a One-Pot Sol-Gel Method for Selective Catalytic Reduction of NO with NH3, Materials 13 (2020), https://doi.org/10.3390/ma13020475.
[54] N. Grifasi, F.A. Deorsola, D. Fino, M. Piumetti, Mesoporous TiO2 and Fe-Containing TiO2 prepared by solution combustion synthesis as catalysts for the photodegradation of paracetamol, Environ. Sci. Pollut. Res. 31 (2024) 36861–36881.
[55] S. Liu, A. Li, C. Yang, F. Ouyang, J. Zhou, X. Liu, MnO2/Mn2O3 with self-triggered oxygen-defects for superior pseudocapacitive energy storage, Appl. Surf. Sci. 571 (2022) 151306.
[56] Y. Zhu, Z. Chen, H. Li, Q. Wang, X. Liu, Y. Hu, C. Su, R. Duan, S. Chen, L. Lan, Effect of Oxygen Vacancy and Highly Dispersed MnO x on Soot Combustion in Cerium Manganese Catalyst, Sci. Rep. 13 (2023) 3386.
[57] Y. Wu, A. Wang, H. Zhao, Q. Zhang, D. Lei, C. Han, Oxygen-Dependent Catalytic Activity of Mesoporous MnCO3-Based Catalysts for Highly Effective Benzene Oxidation, Fuel 363 (2024) 130886.
[58] H. He, X. Lin, S. Li, Z. Wu, J. Gao, J. Wu, W. Wen, D. Ye, M. Fu, The Key Surface Species and Oxygen Vacancies in MnOx (0.4)-CeO2 toward Repeated Soot Oxidation, Appl. Catal. B 223 (2018) 134–142.
[59] L. Zhang, Y. Ding, S. Wang, Insights into the roles of surface oxygen species of manganese oxides for the ozone elimination at ambient temperature, Author Prepr. (2020).
[60] I. Platzman, R. Brener, H. Haick, R. Tannenbaum, Oxidation of polycrystalline copper thin films at ambient conditions, J. Phys. Chem. C. 112 (2008) 1101–1108.
[61] V.N. Popok, S.M. Novikov, Y.Y. Lebedinskij, A.M. Markeev, A.A. Andreev, I. N. Trunkin, A.V. Arsenin, V.S. Volkov, Gas-Aggregated Copper Nanoparticles with Long-Term Plasmon Resonance Stability, Plasmonics 16 (2021) 333–340.
[62] H. Guzmán, J. Albo, A. Irabien, M. Castellino, S. Hernández, Role of Electrochemical Cell Configuration on the Selectivity of CuZnAl-Oxide-Based Electrodes for the Continuous CO2 Conversion: Aqueous Electrolyte vs. Catholyte-Less Configuration, Discov. Chem. Eng. 4 (2024) 12.
[63] L. Meda, G.F. Cerofolini, A Decomposition Procedure for the Determination of Copper Oxidation States in Cu-zeolites by XPS, Surface Interface Analysis International Journal devoted development application techniques analysis surfaces interfaces thin films 36 (2004) 756–759.
[64] M.C. Biesinger, L.W.M. Lau, A.R. Gerson, R.S.C. Smart, Resolving Surface Chemical States in XPS Analysis of First Row Transition Metals, Oxides and Hydroxides: Sc, Ti, V, Cu and Zn, Appl. Surf. Sci. 257 (2010) 887–898.
[65] M.C. Biesinger, Advanced Analysis of Copper X-ray Photoelectron Spectra, Surf. Interface Anal. 49 (2017) 1325–1334.
[66] E. Bojestig, Y. Cao, L. Nyborg, Surface Chemical Analysis of Copper Powder Used in Additive Manufacturing, Surf. Interface Anal. 52 (2020) 1104–1110.
[67] M.J. Marin Figueredo, T. Andana, S. Bensaid, M. Dosa, D. Fino, N. Russo, M. Piumetti, Cerium–Copper–Manganese Oxides Synthesized via Solution Combustion Synthesis (SCS) for Total Oxidation of VOCs, Catal. Lett. 150 (2020) 1821–1840, https://doi.org/10.1007/s10562-019-03094-x.
[68] J. Wang, H. Zhao, J. Song, T. Zhu, W. Xu, Structure-Activity Relationship of Manganese Oxide Catalysts for the Catalytic Oxidation of (Chloro)-VOCs, Catalysts 9 (2019) 726.
[69] J.H. Park, D.C. Kang, S.J. Park, C.H. Shin, CO Oxidation over MnO2 Catalysts Prepared by a Simple Redox Method: Influence of the Mn (II) Precursors, J. Ind. Eng. Chem. 25 (2015) 250–257, https://doi.org/10.1016/j.jiec.2014.11.001.
[70] Y. Liu, H. Zhou, R. Cao, X. Liu, P. Zhang, J. Zhan, L. Liu, Facile and Green Synthetic Strategy of Birnessite-Type MnO2 with High Efficiency for Airborne Benzene Removal at Low Temperatures, Appl. Catal. B 245 (2019) 569–582, https://doi.org/10.1016/j.apcatb.2019.01.023.
[71] S.C. Kim, W.G. Shim, Catalytic Combustion of VOCs over a Series of Manganese Oxide Catalysts, Appl. Catal. B 98 (2010) 180–185, https://doi.org/10.1016/j.apcatb.2010.05.027.
[72] J. Wang, H. Zhao, J. Song, T. Zhu, W. Xu, Structure-Activity Relationship of Manganese Oxide Catalysts for the Catalytic Oxidation of (Chloro)-VOCs, Catalysts 9 (2019), https://doi.org/10.3390/catal9090726.
[73] Y. Meng, Q. Wang, J. Yan, J. Fan, H. Liu, Y. Dai, H. Three-Dimensional Mesoporous Manganese Oxides and Cobalt Oxides: High-Efficiency Catalysts for the Removal of Toluene and Carbon Monoxide, Microporous Mesoporous Mater. 162 (2012) 199–206, https://doi.org/10.1016/j.micromeso.2012.06.030.
[74] Y. Yongnian, H. Ruili, C. Lin, Z. Jiayu, Redox Behavior of Trimanganese Tetroxide Catalysts, Appl. Catal. A Gen. 101 (1993) 233–252.
[75] T.T.T. Hien, L.B. Thuy, P.T.M. Phuong, L.M. Thang, Investigation of CuMnOx Spinel Catalyst for Toluene Oxidation, Vietnam J. Catal. Adsorpt. 10 (2021) 56–62.
[76] M.J.M. Figueredo, M. Piumetti, D. Fino, N. Russo, C. Cocuzza, S. Bensaid, Catalytic Oxidation of Soot and Volatile Organic Compounds over Cu and Fe Doped Manganese Oxides Prepared via Sol-Gel Synthesis, SAE Technical Paper, 2021.
[77] L. Cai, Z. Hu, P. Branton, W. Li, The Effect of Doping Transition Metal Oxides on Copper Manganese Oxides for the Catalytic Oxidation of CO, Chin. J. Catal. 35 (2014) 159–167.
[78] H. Chen, X. Tong, Y. Li, Mesoporous Cu–Mn Hopcalite Catalyst and Its Performance in Low Temperature Ethylene Combustion in a Carbon Dioxide Stream, Appl. Catal. A Gen. 370 (2009) 59–65.
[79] J. Zeng, H. Xie, Z. Liu, X. Liu, G. Zhou, Y. Jiang, Oxygen Vacancy Induced MnO 2 Catalysts for Efficient Toluene Catalytic Oxidation, Catal. Sci. Technol. 11 (2021) 6708–6723.
[80] Y. Ma, Y. Li, P. Liang, X. Min, T. Sun, SnO2-Modified CuMnOx Catalysts for Humid CO Oxidation at Low Temperature, J. Ind. Eng. Chem. 138 (2024) 300–310.
[81] S. ZHANG, A.N. Kang, L.I.U. Yuan, Cu1. 5Mn1. 5O4 Spinel Type Composite Oxide Modified with CuO for Synergistic Catalysis of CO Oxidation, J. fuel Chem. Technol. 49 (2021) 799–808.
[82] Y. Qi, C. Li, H. Li, H. Yang, J. Guan, Elimination or Removal of Ethylene for Fruit and Vegetable Storage via Low-Temperature Catalytic Oxidation, J. Agric. Food Chem. 69 (2021) 10419–10439.
[83] G. Pampararo, E. Sartoretti, A.S. Traoré, O. Ersen, C. Novara, S. Bensaid, D. P. Debecker, Spray-Made Porous CuO-CeO2 Microspheres Rival Precious Metal Catalysts for the Low-Temperature Oxidation of Air Pollutants, J. Environ. Chem. Eng. (2025) 116753.
[84] Q. Zhang, J. Li, S. Chen, C. Zhu, Y. Li, G. Zhao, Co-Assembly of Microfibrous-Structured Ag@ SiO2-Co3O4/Al-Fiber Catalysts Assisted with Water-Soluble Silane Coupling Agent for Catalytic Combustion of Trace Ethylene, Catal. Today 405 (2022) 159–167.
[85] Q. Zhang, L. Zhang, L. Liu, W. Li, C. Zhu, W. Liu, Zr-Doped CoZrOx Solid Solution Catalysts with Enhanced Oxygen Vacancy for Trace Ethylene Removal under Humid Conditions, Appl. Surf. Sci. 689 (2025) 162449.
[86] R. Gui, J. Xiao, Y. Gao, Y. Li, T. Zhu, Q. Wang, Simultaneously Achieving Selective Catalytic Reduction of NOx with NH3 and Catalytic Oxidation of CO with O2 over One Finely Optimized Bifunctional Catalyst Mn2Cu1Al1Ox at Low Temperatures, Appl. Catal. B 306 (2022) 121104.
[87] C.-H. Weng, C.-Y. Liao, J.-H. Tzeng, Y.-C. Chen, J. Anotai, Y.-T. Lin, Constructing Oxygen Vacancy Induced Fe-Mn-Cu Mixed Oxides for Efficient Catalytic Combustion of Ethylene, Appl. Surf. Sci. 631 (2023) 157555.
[88] W. Yu, S. Yue, M. Yang, M. Hashimoto, P. Liu, L. Zhu, W. Xie, T. Jones, M. Willinger, X. Huang, Operando TEM Study of a Working Copper Catalyst during Ethylene Oxidation, Nat. Commun. 16 (2025) 2029.
[89] S. Hu, M. Huang, J. Li, J. He, K. Xu, X. Rao, D. Cai, G. Zhan, Tailoring the Electronic States of Pt by Atomic Layer Deposition of Al2O3 for Enhanced CO Oxidation Performance: Experimental and Theoretical Investigations, Appl. Catal. B Environ. Energy 333 (2023) 122804.
[90] J. Dong, Y. Zhang, D. Li, A. Adogwa, S. Huang, M. Yang, J. Yang, Q. Jin, Reaction-Driven Evolutions of Pt States over Pt-CeO2 Catalysts during CO Oxidation, Appl. Catal. B 330 (2023) 122662.
[91] M. Ghiassee, M. Rezaei, F. Meshkani, S. Mobini, Preparation of the Mn/Co Mixed Oxide Catalysts for Low-Temperature CO Oxidation Reaction, Environ. Sci. Pollut. Res. 28 (2021) 379–388.
[92] J. Li, Y. Lei, Z. Guo, G. Li, X. Chen, F. Zhou, Temperature-Dependent Reaction Pathways of CO Oxidation and the Application as Monolithic Catalysts for Co3O4 Nanorods, Appl. Catal. A Gen. 587 (2019) 117191.
[93] S. Dey, G.C. Dhal, D. Mohan, R. Prasad, Effect of Various Metal Oxides Phases Present in CuMnOx Catalyst for Selective CO Oxidation, Mater. Discov. 12 (2018) 63–71.
[94] U.R. Pillai, S. Deevi, Room Temperature Oxidation of Carbon Monoxide over Copper Oxide Catalyst, Appl. Catal. B 64 (2006) 146–151, https://doi.org/10.1016/j.apcatb.2005.11.005.
[95] H.J. Lee, J.H. Yang, J.H. You, B.Y. Yoon, Sea-Urchin-like Mesoporous Copper-Manganese Oxide Catalysts: Influence of Copper on Benzene Oxidation, J. Ind. Eng. Chem. 89 (2020) 156–165.
[96] C. Jin, W. Si, Y. Chen, X. Zhao, B. Zhou, Y. Shen, Q. Zhu, Y. Chu, F. Liu, M. Li, Enhancing CO Catalytic Oxidation Performance over Cu-Doping Manganese Oxide Octahedral Molecular Sieves Catalyst, J. Colloid Interface Sci. 663 (2024) 541–553.
[97] K. Yu, L. Lou, S. Liu, W. Zhou, Asymmetric Oxygen Vacancies: The Intrinsic Redox Active Sites in Metal Oxide Catalysts, Adv. Sci. 7 (2020) 1901970.
[98] H. Li, Z. Xiao, P. Liu, H. Wang, J. Geng, H. Lei, O. Zhuo, Interfaces and Oxygen Vacancies-Enriched Catalysts Derived from Cu-Mn-Al Hydrotalcite towards High-Efficient Water–Gas Shift Reaction, Molecules 28 (2023) 1522.
[99] N.D. Wasalathanthri, T.M. SantaMaria, D.A. Kriz, S.L. Dissanayake, C.H. Kuo, S. Biswas, S.L. Suib, Mesoporous Manganese Oxides for NO2 Assisted Catalytic Soot Oxidation, Appl. Catal. B 201 (2017) 543–551, https://doi.org/10.1016/j.apcatb.2016.08.052.
[100] A. Davó-Quiñonero, M. Navlani-García, D. Lozano-Castello, A. Bueno-López, J. A. Anderson, Role of Hydroxyl Groups in the Preferential Oxidation of CO over Copper Oxide–Cerium Oxide Catalysts, ACS Catal. 6 (2016) 1723–1731.
[101] E.C. Njagi, H.C. Genuino, C.K. King'ondu, S. Dharmarathna, S.L. Suib, Catalytic oxidation of ethylene at low temperatures using porous copper manganese oxides, Appl. Catal. A Gen. 421 (2012) 154–160.
[102] W. Wei, Z. Wei, R. Li, Z. Li, R. Shi, S. Ouyang, Y. Qi, D.L. Philips, H. Yuan, Subsurface oxygen defects electronically interacting with active sites on In2O3 for enhanced photothermocatalytic CO2 reduction, Nat. Commun. 13 (2022) 3199.
[103] K. Shen, C.-Y. Wang, R.K. Rai, E.A. Stach, J.M. Vohs, R.J. Gorte, Synthesis of thin-film CuMn2O4 for low-temperature CO oxidation, Appl. Catal. A Gen. 682 (2024) 119823.
[104] Y. Zhang, Y. Lin, T. Duan, L. Song, Interfacial engineering of heterogeneous catalysts for electrocatalysis, Mater. Today 48 (2021) 115–134.
[105] C.G. Vayenas, S. Bebelis, S. Ladas, Dependence of catalytic rates on catalyst work function, Nature 343 (1990) 625–627.

[106] L. Lin, R. Jacobs, T. Ma, D. Chen, J. Booske, D. Morgan, Work function: fundamentals, measurement, calculation, engineering, and applications, Phys. Rev. Appl. 19 (2023) 37001.
[107] K. Morgan, K.J. Cole, A. Goguet, C. Hardacre, G.J. Hutchings, N. Maguire, S. O. Shekhtman, S.H. Taylor, TAP Studies of CO Oxidation over CuMnOX and Au/CuMnOX Catalysts, J. Catal. 276 (2010) 38–48.
[108] Z. He, B. Zheng, Microscopic Investigation of CO Oxidation Reaction by Copper–Manganese Oxide Catalysts, Catal. Lett. 155 (2025) 4.
[109] J. Bao, X. Duan, P. Zhang, Facile Synthesis of a CuMnO x Catalyst Based on a Mechanochemical Redox Process for Efficient and Stable CO Oxidation, J. Mater. Chem. A Mater. 8 (2020) 24438–24444.
[110] P. Zhang, H. Lu, Y. Zhou, L. Zhang, Z. Wu, S. Yang, H. Shi, Q. Zhu, Y. Chen, S. Dai, Mesoporous MnCeO x Solid Solutions for Low Temperature and Selective Oxidation of Hydrocarbons, Nat. Commun. 6 (2015) 8446.
[111] T. Liu, Y. Yao, L. Wei, Z. Shi, L. Han, H. Yuan, B. Li, L. Dong, F. Wang, C. Sun, Preparation and Evaluation of Copper–Manganese Oxide as a High-Efficiency Catalyst for CO Oxidation and NO Reduction by CO, J. Phys. Chem. C. 121 (2017) 12757–12770.
[112] Y. Sun, R. Zhu, G. Bai, T. Xin, J. Li, X. Zhou, W. Chang, J. Wang, M. Xiao, Study on the Catalytic Mechanism and Water Resistance of Cu-Mn-Snx Catalyst for CO Elimination, Sci. Rep. 15 (2025) 3775.
[113] M. Piumetti, B. Bonelli, P. Massiani, Y. Millot, S. Dzwigaj, L. Gaberova, M. Armandi, E. Garrone, Novel Vanadium-Containing Mesocellular Foams (V-MCF) Obtained by Direct Synthesis, Microporous Mesoporous Mater. 142 (2011) 45–54.
[114] X. Gong, J. Xu, T. Zhang, Y. Sun, S. Fang, N. Li, J. Zhu, Z. Wu, J. Li, E. Gao, DRIFTS-MS Investigation of Low-Temperature CO Oxidation on Cu-Doped Manganese Oxide Prepared Using Nitrate Aerosol Decomposition, Molecules 28 (2023) 3511.
[115] Mezzapesa M. Pietro, F. Salomone, E. Sartoretti, R. Pirone, S. Bensaid, F. C. Meunier, Decrease in DRIFTS Optical Path Length Induced by Sample Reduction Led to Cu–Ce Phase Being IR-Invisible, J. Phys. Chem. C. 129 (2025) 8974–8984.
[116] M. Arduino, E. Sartoretti, E. Calì, S. Bensaid, F.A. Deorsola, Understanding the RolE of Morphology in the Direct Synthesis of Diethyl Carbonate over Ceria-based Catalysts: An In Situ infrared and high-resolution TEM study, ChemCatChem (2025) e00140.
[117] A. Rizzetto, M. Piumetti, R. Pirone, E. Sartoretti, S. Bensaid, Study of ceria-composite materials for high-temperature CO2 capture and their ruthenium functionalization for methane production, Catal. Today 429 (2024) 114478, https://doi.org/10.1016/j.cattod.2023.114478.
[118] H. Gu, J. Lan, Y. Liu, C. Ling, K. Wei, G. Zhan, F. Guo, F. Jia, Z. Ai, L. Zhang, Water enables lattice oxygen activation of transition metal oxides for volatile organic compound oxidation, ACS Catal. 12 (2022) 11272–11280.
[119] D. Pankin, M. Smirnov, A. Povolotckaia, A. Povolotskiy, E. Borisov, M. Moskovskiy, A. Gulyaev, S. Gerasimenko, A. Aksenov, M. Litvinov, DFT Modelling of Molecular Structure, Vibrational and UV-Vis Absorption Spectra of T-2 Toxin and 3-Deacetylcalonectrin, Materials 15 (2022) 649.
[120] H.-J. Freund, Model studies on heterogeneous catalysts at the atomic level, Catal. Today 100 (2005) 3–9.
[121] Z. Hou, M. Chen, Y. Liu, J. Deng, L. Jing, R. Gao, W. Pei, Z. Li, H. Dai, Enhanced moisture resistance and catalytic stability of ethylene oxidation at room temperature by the ultrasmall MnOx Cluster/Pt hetero-junction, Appl. Catal. B 339 (2023) 123115.
[122] Y. Dong, F. Wang, W. Song, P. Wang, C. Zhu, X. Wang, S. Li, X. Li, W. Li, Construction of surface oxygen vacancy active sites upon MnOx/AC composite catalysts for efficient coupling adsorption and oxidation of toluene, Chem. Eng. J. 464 (2023) 142740.